Evaluating turbulent channel flows with rough walls

Homogeneous roughness parameterization for use in a map-based turbulence model

Medina Méndez, Juan A.; Klein, Marten; Peeters, Jurriaan W.R.; Schmidt, Heiko

DOI
10.1016/j.ijheatfluidflow.2025.110113

Publication date
2026

Document Version
Final published version

Published in
International Journal of Heat and Fluid Flow

International Journal of Heat and Fluid Flow 117 (2026) 110113

Contents lists available at ScienceDirect

International Journal of Heat and Fluid Flow

journal homepage: www.elsevier.com/locate/ijhff

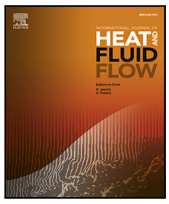

Evaluating turbulent channel flows with rough walls: Homogeneous roughness parameterization for use in a map-based turbulence model☆

Juan A. Medina Méndez [a,*], Marten Klein [a], Jurriaan W.R. Peeters [b], Heiko Schmidt [a]

[a] BTU Cottbus-Senftenberg, Chair of Numerical Fluid and Gas Dynamics, Siemens-Halske-Ring 15a, Cottbus, 03046, Brandenburg, Germany
[b] Delft University of Technology, Energy Technology, Leeghwaterstraat 39, Delft, 2628 CB, Netherlands

ARTICLE INFO

Keywords:
Turbulent channel
Roughness
ODT
Volume-averaging

ABSTRACT

This work is focused on modeling the effects of homogeneous roughness on low-order velocity statistics in turbulent channel flows. Hydrodynamic effects due to the roughness are characterized on the basis of volume-averaging theory (VAT) and a discrete roughness element method. This theory exploits the homogeneous character of the roughness in order to reduce the complexity of the flow to its one-dimensional statistics. The formulated VAT-based roughness forcing is best suited for drag dominated surfaces. Turbulence modeling closure is achieved with a map-based turbulence model, the One-Dimensional Turbulence (ODT) model. This avoids the prescription of laws of the wall or other ad-hoc scalings, unlike in more traditional filter-based turbulence models. The modeling framework is applied on selected Reynolds number flows for likewise selected roughness topologies. Results are compared to direct numerical simulation (DNS) data available from the literature. Among others, model results are compared with those of a previously formulated parametric forcing approach (PFA) for roughness drag which involved a costly coefficient calibration linked to the roughness topology model. In ODT, the only calibration process required is the same one involved for the turbulence model parameters, i.e., similar to the ODT model application for smooth-wall flows. Despite all of the inherently implied shortcomings of a 1-D model, some appealing properties of ODT are discussed. Notably, the model is able to predict the roughness function, as well as the wall-normal profile of the Reynolds shear stress across the entire boundary layer thickness.

1. Research context, significance, and outline of the work

The interactions between rough surfaces and turbulent flows are studied in a wide variety of disciplines. The atmospheric boundary layer over canopies or buildings is a related formal topic in atmospheric sciences (Cooke et al., 2024), civil and structural engineering (Toja-Silva et al., 2018), and similar. Corrosion can also be considered as a closely related formal discipline for more technical applications, see Thorat et al. (2024). The exact prediction of the drag generated by a specific rough surface at arbitrary flow conditions may probably be one of the most relevant parameters of concern when predicting associated fluid flows. This has been an important rationale when studying flows over rough surfaces, best exemplified by the early ideas proposed by Nikuradse (1933), and later operationalized by Schlichting (1937) in the concept of sand-grain roughness height. The shortcoming in that concept being that the sand-grain roughness height cannot be directly related to the roughness geometry.

Understanding of roughness and turbulence interactions at a fundamental level should ideally be achieved by a joint effort of DNS and experimental work. For DNS, the representation of the roughness surface topology is usually done by means of techniques such as conformal mappings or immersed boundary methods (Mittal and Iaccarino, 2005; Busse et al., 2015). Accurate topology representations imply expensive simulation costs, and as such, there are not that many DNS publications in which roughness topology parameters are systematically varied (Chan et al., 2015; Busse et al., 2017). Experimental work is not as strictly limited as DNS, however, relevant publications with systematic parametric investigations are also not that common (Schultz and Flack, 2009; Flack et al., 2020a,b). An alternative to accurate roughness surface topology representation in DNS can be obtained by modeling the rough surface with the use of the method of discrete roughness elements, for which it is also possible to further reduce computational costs associated with numerical simulations by the use of turbulence modeling strategies, see e.g., McClain and Brown (2009), Forooghi et al. (2017), Hanson et al. (2019), Chedevergne (2021) and Chedevergne et al. (2025).

☆ This article is part of a Special issue entitled: 'TSFP13' published in International Journal of Heat and Fluid Flow.

* Corresponding author.
E-mail address: medinjua@b-tu.de (J.A. Medina Méndez).

https://doi.org/10.1016/j.ijheatfluidflow.2025.110113
Received 31 January 2025; Received in revised form 15 October 2025; Accepted 15 October 2025
Available online 31 October 2025

Nomenclature

English symbols

C	ODT eddy rate parameter
$\hat{c}_I, \hat{c}_{II}, \hat{c}_{III}$	VAT-based drag-related forcing coefficients
$\mathcal{C}$	Intersection between the REV and the roughness surface at given y
C_f	Skin friction coefficient
c_i	ODT kernel coefficients for all velocity components, $i \in \{1,2,3\}$
$D_\circ$	Equivalent cylinder diameter of the discrete roughness elements
D_k	Equivalent pore diameter
e_d	Loss of kinetic energy due to drag during eddy events
e_K	Change in kinetic energy during eddy events
ES	Roughness surface effective slope
$\overline{f_{pd}}$	Statistically stationary total interfacial stress modeled by double-averaged velocity field
$\overline{f_p}$	(Long-)Time-averaged f_p
$f(y)$	Triplet-map function
f_p	VAT-related C-contour-averaged total interfacial stress modeled by volume-averaged velocity field
G	Nondimensional pressure gradient due to staggered cylinder array for volume-averaged flow
$\overline{G}$	Nondimensional pressure gradient due to staggered cylinder array for double-averaged flow
G_0	Nondimensional Darcy-flow pressure gradient
H	Half-height of the channel measured from roughness trough
$\mathcal{I}$	VAT-related inhomogeneous porosity term
$\overline{\mathcal{I}}$	Statistically stationary inhomogeneous porosity term
$\mathcal{J}_{D,xx}$	Darcy permeability for 1-D streamwise flow
$\mathcal{J}_T$	Total permeability tensor for volume-averaged flow
K	ODT kernel function
k	Average roughness height
$\mathcal{K}$	Turbulence kinetic energy (TKE)
$\overline{\mathcal{J}_T}$	Total permeability tensor for double-averaged flow
$\widetilde{k}(x,z)$	Roughness surface topology
k_{MD}	Meltdown roughness height (*a priori* virtual wall location)
k_{RMS}	Root-mean-square roughness height
$k_{\max}$	Roughness crest height
$k_{\min}$	Roughness trough height ($y = 0$)
k_{ref}	Reference roughness height for *a posteriori* virtual wall location
L	Numerical domain length
l	ODT eddy event length
$L_{\overline{\pi}}$	Length of the representative elementary volume (averaging plane)
$\mathcal{M}$	Triplet map operation on a 1-D scalar velocity profile
$\overline{\mathcal{M}_{\mathcal{N}}}$	Alternative ODT notation for double-averaged Reynolds shear stress gradient $\partial\overline{\langle v'u_i'\rangle}/\partial y$
N_k	Total number of equivalent circular discrete elements representing fluid-phase area
N_T	Total number of cylindrical roughness elements
P	TKE production
p	Pressure
$\hat{P}$	TKE production peak
$p_\circ$	Pressure drop due to drag of one cylinder
Re_p	Pore Reynolds number
Re_τ	Friction Reynolds number
S_k	Roughness surface (normalized) skewness
t	Time
t_l	Turnover time of eddy event
$\langle \overline{u_i''}\ \overline{u_j''} \rangle$	Mechanical dispersion term for double-averaged flow
$\langle u_i'' u_j'' \rangle$	Residual subgrid-stress-like tensor, VAT-related dispersion
$\overline{\langle u_i' u_j' \rangle}$	Double-averaged Reynolds stresses (turbulent dispersion)
u, v, w	Alternative notation for $u_i, \quad i \in \{1,2,3\}$
$U^{+(\mathrm{MD,ref})}$	Roughness function-related velocity, normalized using either the *a priori* or the *a posteriori* virtual wall location and scalings
u_τ	Friction velocity
U_b	Bulk flow velocity
u_i	Streamwise, wall-normal, and spanwise velocity components, $i \in \{1,2,3\}$
W	Numerical domain width
$\mathcal{W}$	Weibull PDF-fit for statistical reconstruction of a roughness surface
$W_{\overline{\pi}}$	Width of the representative elementary volume (averaging plane)
x, y, z	Alternative notation for x_i
x_i	Streamwise, wall-normal, and spanwise coordinates, $i \in \{1,2,3\}$
$y_{\overline{\pi}}$	Wall-normal position or thickness of the REV (averaging plane)
Z	ODT small-scale viscous suppression parameter

Greek symbols

α	ODT pressure-scrambling parameter
β	Forchheimer-regime related coefficient for G
χ	Fluid phase indicator function
Δ	Relative quantity
δ_ν	Viscous length-scale
$\delta_{i\neq j}$	Alternative Delta operator (1 if $i \neq j$, and 0 otherwise, $i, j \in \{1,2,3\}$)
δ_{ij}	Delta operator (1 if $i = j$, and 0 otherwise, $i, j \in \{1,2,3\}$)
ϵ	Fluid phase porosity ($\epsilon = 1$ is homogeneous fluid phase)
γ_t	Transition-regime related coefficient for G
μ	Fluid dynamic viscosity

ν	Fluid kinematic viscosity
ϕ	Shape parameter for the Weibull PDF-fit characterizing the roughness
ψ	Power law distribution (with fractional exponent) of stochastic roughness element heights
ρ	Fluid density
τ	Total or shear stress (depending on corresponding subscript)
θ	Scale parameter for the Weibull PDF-fit characterizing the roughness
ε	TKE dissipation rate
ζ	Hydrodynamic FPG driving the flow ($-\zeta > 0$)

Operators

$\langle\cdot\rangle$	Volume-average operator
$\langle\cdot\rangle^{\sigma}$	Intrinsic (volume-)average operator, $\langle\cdot\rangle^{\sigma} = \langle\cdot\rangle/\epsilon$
$\|\|\cdot\|\|$	Vector magnitude
$\bar{\cdot}$	(Long) Time-average operator
$\overline{\langle\cdot\rangle}$	Double-average operator
$\partial/\partial t$	Partial derivative with respect to time
$\partial/\partial x, \partial/\partial y, \partial/\partial z$	Alternative notation for streamwise, wall-normal, and spanwise gradient operator
$\partial/\partial x_i$	Streamwise, wall-normal, and spanwise gradient operator, $i \in \{1,2,3\}$
$''$	Residual or deviation between local and intrinsic averaged quantity
$'$	Fluctuation or deviation between instantaneous and (long-)time-averaged quantity

Subscripts and superscripts

$+$	Viscous or wall scaling
MD	*A priori* scaling or related quantity set by virtual wall location at the meltdown roughness height
ref	Scaling or quantity set by *a posteriori* virtual wall location
D	Darcy-flow related quantity
i	$i \in \{1,2,3\}$, Cartesian vector components
j	$j \in \{1,2,3\}$, Cartesian vector components
w	Wall-related
tot	Total

Abbreviations

CDF	Cumulative distribution function
DANS	Double-averaged Navier-Stokes
DNS	Direct numerical simulation
FPG	Fixed pressure gradient
LES	Large eddy simulation
LHS	Left-hand side
LVM	Large-scale cavity vortex model
ODT	One-Dimensional Turbulence
PDF	Probability density function
PFA	Parametric forcing approach
RANS	Reynolds-averaged Navier-Stokes
REV	Representative elementary volume
RHS	Right-hand side
TKE	Turbulence kinetic energy
VAT	Volume-averaging theory
VLES	Very large eddy simulation

We pursue a numerical approach to study roughness and turbulence interactions which resorts to turbulence modeling instead of DNS, despite all of the potential inherent limitations. The majority of economical filter-based turbulence models, such as Reynolds-averaged Navier–Stokes (RANS) or very large eddy simulation (VLES), rely on approximations to the law of the wall in order to provide correct near-wall behavior of the averaged flow (Pope, 2001). Such approximations are not well understood for rough walls, see Chung et al. (2021). This is an important limitation for said filter-based approaches, and it is the reason why we propose instead the use of a map-based turbulence model, ODT (Kerstein, 1999), which is not directly related to the use of filter operators on the Navier–Stokes equations. The ODT rationale is based on ergodicity theory and the way in which maps, such as Baker's maps, are an example of strong mixing (Sturman, 2012). Origins of the use of maps for understanding or explaining turbulence phenomenology can be traced back to Chorin (1986), or even before to Reynolds himself (Ottino et al., 1994). Specifically, ODT relies on a specific type of mapping, a triplet map on 1-D scalar profiles (Kerstein, 1999), in order to represent turbulent transport. Scaling laws do not need to be prescribed directly in ODT. Rather, they are the result of an ensemble average of mapping implementations, see Klein et al. (2022). In this way, ODT allows us to avoid the use of approximations to the law of the wall which are required in most widespread RANS turbulence models, e.g., $\mathcal{K}-\omega$ models, or alternatively, the use of heuristic damping functions for near-wall asymptotic consistency as in so-called low Reynolds numbers models utilizing viscous sublayer resolution, e.g., the Launder-Sharma $\mathcal{K}-\varepsilon$ model (Wilcox, 2006).

In the present modeling framework to study turbulent channel flows with homogeneous roughness, the representation of the roughness is achieved with a discrete roughness elements method (McClain and Brown, 2009; Forooghi et al., 2017; Hanson et al., 2019; Chedevergne, 2021; Altland, 2022; Chedevergne et al., 2025). In said family of approaches, the hydrodynamic effect of the roughness is represented as an equivalent body force in the governing equations (Aupoix, 2015; Chedevergne, 2021; Chedevergne et al., 2025). We evaluate the performance of our model with numerical simulations at selected Reynolds numbers for likewise selected different roughness topologies. Finally, we comment on the obtained results and offer an outlook on potential future work for model improvement, or for more practical applications.

2. Roughness-drag characterization and forcing

We conceptualize the homogeneous roughness as being originated by a set of discrete roughness elements. We are interested in deriving a 1-D wall-normal forcing representation for the roughness drag, which can be obtained by the application of VAT, similar to previous studies (Aupoix, 2015; Chedevergne, 2021; Chedevergne et al., 2025). Although we do not intend to solve double-averaged Navier–Stokes (DANS) equations directly unlike previous studies, for the purpose of generality and better understanding of our approach, we discuss the derivation of said DANS equations next. Afterwards, we explain our strategy for turbulence modeling closure utilizing the alternative map-based ODT model.

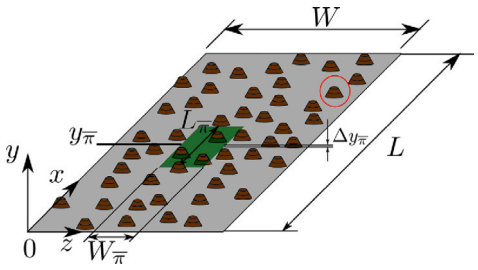

Fig. 1. Averaging plane and discrete roughness elements.

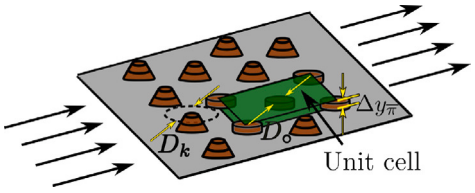

Fig. 2. Intersection between averaging plane and roughness elements, showing the ideal REV (unit cell with a staggered cylinder array).

2.1. Double-averaged Navier–Stokes equations

We define an averaging plane $\overline{\pi}$, or equivalently, a REV of thickness $\Delta y_{\overline{\pi}}$, length $L_{\overline{\pi}} \ll L$ and width $W_{\overline{\pi}} \ll W$, where L and W are the length and width of the numerical domain, respectively, see Fig. 1. The thickness $\Delta y_{\overline{\pi}}$ is set in such a way that it corresponds to the numerical resolution of our simulation, which should be capable of resolving the Kolmogorov scale of the turbulent flow. It is noted that the roughness elements shown in Fig. 1 may have any arbitrary shape. However, the ideal approximation anticipated in our framework is obtained when the intersection between the averaging plane and the roughness elements yields a staggered array of (almost flat) cylindrical sections (or rather, truncated cones which can be approximated as almost flat cylinders), see Fig. 2. If D_k, an equivalent diameter open to the fluid, is a pore scale as in Fig. 2, then classical VAT assumptions hold in the sense that $\pi D_k^2/4 \ll \sqrt{L_{\overline{\pi}} W_{\overline{\pi}}} \ll \sqrt{LW}$ (Whitaker, 1999; Aupoix, 2015). These considerations are similar to those of the model proposed by Chedevergne (2021).

We define the volume average of the velocity field $u_i(x, y, z, t)$, for $i \in \{1, 2, 3\}$, and the pressure $p(x, y, z, t)$,

$$\begin{aligned} \langle u_i \rangle(x, y, z, t) &= \frac{1}{L_{\overline{\pi}} W_{\overline{\pi}}} \iint_{\overline{\pi}} u_i \chi \, \mathrm{d}z\mathrm{d}x, \\ \langle p \rangle(x, y, z, t) &= \frac{1}{L_{\overline{\pi}} W_{\overline{\pi}}} \iint_{\overline{\pi}} p \chi \, \mathrm{d}z\mathrm{d}x. \end{aligned} \tag{1}$$

We use the alternative index notation with $i = 1$ as the streamwise direction $x_1 = x$ and aligned velocity component $u_1 = u$, $i = 2$ as the wall-normal direction $x_2 = y$ with aligned velocity component $u_2 = v$, and $i = 3$ as the spanwise direction $x_3 = z$ with aligned velocity component $u_3 = w$. In Eq. (1), χ is a unitary indicator function which is only nonzero within the fluid phase, which we will reference as σ. Note that the volume average is defined with a double integration. This is because flow variables are assumed constant in y within the REV (up to numerical accuracy), in such a way that integrals in y are redundant. We define the intrinsic average of the fluid phase as $\langle u_i \rangle^\sigma = \langle u_i \rangle / \epsilon$ and $\langle p \rangle^\sigma = \langle p \rangle / \epsilon$ for the velocity and the pressure, respectively. The porosity of the REV, ϵ, is defined as

$$\epsilon = \frac{1}{L_{\overline{\pi}} W_{\overline{\pi}}} \int_{L_{\overline{\pi}}} \int_{W_{\overline{\pi}}} \chi(x, y, z) \, \mathrm{d}z\mathrm{d}x \approx \frac{1}{LW} \int_L \int_W \chi(x, y, z) \, \mathrm{d}z\mathrm{d}x. \tag{2}$$

This definition of porosity assumes $\epsilon = \epsilon(y)$ to be homogeneous in x and z, mainly due to the homogeneous character of the roughness. As such, $\partial\epsilon/\partial x \approx \partial\epsilon/\partial z \approx 0$. The indicator function χ can be interpreted as a type of negative Heaviside function (since χ is 1 within the phase σ). As such, the double area integral of the gradient $\partial\chi/\partial y$, is equivalent to minus the evaluation of said double integral at the discontinuous points of χ at given y. This is the perimeter of parameterized curves $C(x, z)$ at a given y, or simply $C(x, y, z)$. In terms of porosity, this is

$$\frac{\partial \epsilon}{\partial y} = \frac{1}{LW} \int_L \int_W \frac{\partial \chi(x, y, z)}{\partial y} \, \mathrm{d}z\mathrm{d}x = -\frac{1}{LW} \int_{C(x,y,z)} \mathrm{d}C. \tag{3}$$

All assumptions from classical VAT are considered next, see Whitaker (1999). There is a clear scale separation between the roughness (horizontal) scale, the pore scale $D_k(y)$, and the size of the REV. As such, $D_k(y) \ll \sqrt{L_{\overline{\pi}} \times W_{\overline{\pi}}}$. We focus on the study of canonical channel flows with rough walls. To that extent, we rely conceptually on usual channel flow configurations which employ periodic boundary conditions in the streamwise and spanwise directions, as well as no-slip conditions at the (rough) walls. The rough walls resemble the surface visualized in Fig. 1. The conservation equation for flow momentum, subject to the zero divergence condition of the velocity field for incompressible flow is

$$\frac{\partial u_i}{\partial t} + \frac{\partial \left(u_j u_i \right)}{\partial x_j} = -\zeta \delta_{i1} - \frac{1}{\rho} \frac{\partial p}{\partial x_i} + \nu \frac{\partial}{\partial x_j} \left(\frac{\partial u_i}{\partial x_j} \right), \quad \text{subject to} \quad \frac{\partial u_i}{\partial x_i} = 0. \tag{4}$$

Here, ρ is the (constant) fluid density, and ν is the (constant) kinematic viscosity. As a result of the homogeneous roughness, we expect a statistically homogeneous flow along the directions spanning the rough wall (x and z according to the sketch shown in Fig. 1). In order to drive the channel flow, we consider a fixed (and favorable) time-averaged and uniform hydrodynamic pressure gradient. The latter is noted as $-\zeta$ in Eq. (4), as a way to distinguish it from other pressure gradient terms during the derivation procedure of the DANS equations. In this context, $\zeta < 0$ or $-\zeta > 0$ is a uniform acceleration term in Eq. (4), i.e., a source term for u_1. This explains the use of δ_{i1} in Eq. (4), which is only non-zero for $i = 1$.

Next, the volume averaged version of Eq. (4) is obtained. A decomposition of variables is required as suggested by Whitaker (1999), namely, $u_i = \langle u_i \rangle^\sigma + u_i''$. Double-primed variables represent residual quantities within the REV. The volume-averaged momentum equation is then,

$$\frac{\partial \langle u_i \rangle}{\partial t} = -\frac{\partial \left(\epsilon \langle u_j \rangle^\sigma \langle u_i \rangle^\sigma \right)}{\partial x_j} - \frac{\partial \langle u_j'' u_i'' \rangle}{\partial x_j} - \zeta \delta_{i1} - \frac{1}{\rho} \frac{\partial \langle p \rangle}{\partial x_i} + \nu \frac{\partial^2 \langle u_i \rangle}{\partial x_j^2} + \mathcal{I}_i + f_{p,i}. \tag{5}$$

Several forms of the volume-averaged momentum equation can be found in Breugem (2005). The most relevant form for this work is that in Aupoix (2015). In our specific case, the form of interest of the momentum equation is that of a transport equation for the volume-averaged (or plane-averaged) velocity, instead of usual forms related to the intrinsic-averaged velocity. The exception is an advection term by intrinsic-averaged quantities in Eq. (5), i.e., the first term on the RHS. The term $\langle u_j'' u_i'' \rangle$ is a residual subgrid stress-like term, commonly known as dispersion in the context of VAT (Whitaker, 1996; Breugem, 2005). We have also defined an inhomogeneous porosity term $\mathcal{I}_i$ (assuming $\partial\epsilon/\partial x \approx \partial\epsilon/\partial z \approx 0$), as well as an effort term $f_{p,i}$,

$$\mathcal{I}_i = -\frac{1}{\epsilon} \frac{\partial \epsilon}{\partial y} \left(-\frac{\langle p \rangle}{\rho} \delta_{i2} + \nu \frac{\partial \langle u_i \rangle}{\partial y} - \frac{\nu}{\epsilon} \langle u_i \rangle \frac{\partial \epsilon}{\partial y} \right), \tag{6}$$

$$f_{p,i} = \frac{\delta_{j \neq 2}}{\rho L_{\overline{\pi}} W_{\overline{\pi}}} \int_C \left(-p'' \delta_{ij} + \mu \frac{\partial u_i''}{\partial x_j} \right) \hat{n}_j \, \mathrm{d}C. \tag{7}$$

Note that $\delta_{j \neq 2}$ is zero if $j = 2$ in Eq. (7). The integral term $\int_C \{\} \mathrm{d}C$ in Eq. (7) represents a contour filter, see Whitaker (1996). This is the contour average of the viscous stress and the hydrostatic pressure at the roughness interfaces. We can also obtain a constraint on the volume-averaged velocity field by volume-averaging the divergence condition of the incompressible flow,

$$\frac{\partial \langle u_i \rangle}{\partial x_i} = 0. \tag{8}$$

Similar to Aupoix (2015) and Chedevergne (2021), we are also interested on the ensemble-, or more specifically, (long) time-averaged flow resulting from Eqs. (5) and (8). The time-averaged and volume-averaged flow is inherently one-dimensional, and will help toward our desired 1-D forcing representation for the average roughness drag. Therefore, we formally introduce time-averaged versions of the flow variables as $\overline{u_i}(x,y,z)$ and $\overline{p}(x,y,z)$, as well as double-averaged flow variables $\overline{\langle u_i\rangle}(y)$ and $\overline{\langle p\rangle}(y)$. We also resort to the usual Reynolds decomposition, such that $u_i = \overline{u_i} + u_i'$, and $p = \overline{p} + p'$. The applicable DANS momentum equation, following derivation procedures as in Mignot et al. (2008), Aupoix (2015) and Chedevergne (2021), is

$$0 = -\zeta\delta_{i1} - \frac{1}{\rho}\frac{\partial\overline{\langle p\rangle}}{\partial y}\delta_{i2} + \nu\frac{\partial^2\overline{\langle u_i\rangle}}{\partial y^2} + \overline{\mathcal{I}_i} + \overline{f_{pd,i}} - \frac{\partial\langle\overline{u_2''}\,\overline{u_i''}\rangle}{\partial y} - \frac{\partial\overline{\langle u_2'u_i'\rangle}}{\partial y}. \tag{9}$$

We remark the following definitions for $\overline{f_{pd,i}}$, and for the statistically stationary inhomogeneous porosity term $\overline{\mathcal{I}_i}$,

$$\overline{f_{pd,i}} = \frac{\delta_{j\neq 2}}{\rho L_{\overline{\pi}} W_{\overline{\pi}}}\int_C\left(-\overline{p''}\delta_{ij} + \mu\frac{\partial\overline{u_i''}}{\partial x_j}\right)\hat{n}_j\,\mathrm{d}C, \tag{10}$$

$$\overline{\mathcal{I}_i} = -\frac{1}{\epsilon}\frac{\partial\epsilon}{\partial y}\left(-\frac{\overline{\langle p\rangle}}{\rho}\delta_{i2} + \nu\frac{\partial\overline{\langle u_i\rangle}}{\partial y} - \frac{\nu}{\epsilon}\overline{\langle u_i\rangle}\frac{\partial\epsilon}{\partial y}\right). \tag{11}$$

As in Aupoix (2015), we recognize the term $\overline{f_{pd,i}}$ as the statistically stationary effort term corresponding to a microscopic momentum contour filter in Eq. (9). This is an averaged drag force density for the resulting 1-D DANS flow. The sixth term on the right-hand side (RHS) of Eq. (9) corresponds to an average mechanical dispersion term, see Breugem (2005). Finally, the seventh term is the turbulent dispersion or Reynolds stress term.

2.2. Roughness-drag parameterization

In the limit of negligible mean advection, turbulence (Reynolds stress), and mechanical dispersion, the stationary effort term $\overline{f_{pd,i}}$ can be modeled by means of a scalar Darcy permeability $\mathcal{J}_{D,xx}$ (Mei and Auriault, 1991; Whitaker, 1999). The permeability $\mathcal{J}_{D,xx}$ has units [m^2]. The Darcy flow is the macroscopic steady laminar flow solution of Eq. (9), driven by an equivalent pressure gradient $\rho\zeta_D$,

$$\langle u_1\rangle_D = -\frac{\mathcal{J}_{D,xx}}{\mu\epsilon}\left(\rho\zeta_D\right). \tag{12}$$

As per Eq. (9), the flows of interest for this work consider not only the macroscopic effects of mechanical dispersion, but also the usual effects due to the Reynolds stress. Several studies and authors argue that subfilter-scale mechanical dispersion is normally negligible with respect to the drag force and the Reynolds stress (Breugem, 2005; Breugem et al., 2006). Other authors stress the relevance of adequate consideration and modeling of mechanical dispersion (Toussaint et al., 2020; Chedevergne et al., 2025). Despite the inherent limitations, to be discussed later, we choose to rely on the *standard model* as referenced by Aupoix (2015), in which suitable modeling for a permeability tensor $\mathcal{J}_{T,ij}$ (including corrections to Darcy's law), subsumes the effects of the mechanical dispersion term on the pressure gradient associated to the macroscopic steady flow. This is the reason why we assume the incorporation of $\partial\langle\overline{u_2''}\,\overline{u_i''}\rangle/\partial y$ in our permeability analysis. Therefore, we consider the following relation for the inverse of the permeability tensor of the statistically stationary flow $\overline{\mathcal{J}_{T,ij}}^{-1}$, following ideas from (Whitaker, 1996),

$$-\nu\overline{\mathcal{J}_{T,ij}}^{-1}\,\epsilon\overline{\langle u_j\rangle} \approx -\frac{\partial\langle\overline{u_2''}\,\overline{u_i''}\rangle}{\partial y} + \overline{f_{pd,i}}. \tag{13}$$

We resort to the use of known approximations for $\overline{\mathcal{J}_{T,ij}}$ (or $\mathcal{J}_{T,ij}$), as in Darcy flow-like permeability data which includes corrections due to inertial effects, e.g., the Forchheimer correction term. Such approximations have been extensively studied and discussed in the literature. Despite inherent limitations, we choose to rely on the magnitude of an isotropic permeability for mean streamwise flow $\overline{\mathcal{J}_{T,xx}}$, such that $\overline{\mathcal{J}_{T,ij}} = \overline{\mathcal{J}_{T,xx}}\delta_{ij}$. We assume that the role of $\overline{\mathcal{J}_{T,xx}}$ is that of yielding drag, i.e., a roughness-induced drag. The drag is due to the situation in Fig. 2, i.e., a flow through an array of cylinders. The cylinder array is staggered in the ideal case. The resistance (drag) force is due to the pressure drop by one cylinder $\Delta p_\circ$, multiplied by the cylindrical wall area of one cylinder $\pi D_\circ \Delta y_{\overline{\pi}}$, and the number of cylinders N_T. Reinterpreting $\mathcal{J}_{D,xx}$ as $\overline{\mathcal{J}_{T,xx}}$, and $\langle u_1\rangle_D$ as $\overline{\langle u_1\rangle}$ in Eq. (12), and solving for $\overline{\mathcal{J}_{T,xx}}^{-1}$ using the equivalent pressure drop of the cylinder array, we find

$$\overline{\mathcal{J}_{T,xx}}^{-1} = -\frac{1}{\mu\overline{\langle u_1\rangle}}\left(\frac{N_T\pi D_\circ}{W}\right)\left(\frac{\Delta p_\circ}{L}\right). \tag{14}$$

The nondimensional form of this expression is obtained using the pore diameter, which we note as D_k. With the definition $\Delta p_\circ/L = \mathrm{d}p_\circ/\mathrm{d}x$, we have then the nondimensional permeability

$$D_k^2\overline{\mathcal{J}_{T,xx}}^{-1} = \frac{N_T\pi D_\circ}{W}\overline{G}, \quad \text{where } \overline{G} = -\frac{D_k^2}{\mu\overline{\langle u_1\rangle}}\frac{\mathrm{d}p_\circ}{\mathrm{d}x_1}. \tag{15}$$

$\overline{G}$ is a nondimensional pressure gradient. This analysis is valid for one thin plane representing the situation from Fig. 2, such that $\overline{G}$ can be generalized to a wall-normal profile $\overline{G}(y)$. Similarly, we can define a pore Reynolds number at any y coordinate as

$$\mathrm{Re}_p(y) = \frac{\left\|\overline{\langle u_i\rangle}(y)\right\| D_k(y)}{\nu}. \tag{16}$$

Khalifa et al. (2020) have obtained a quadratic regression for $\overline{G}$ as a function of Re_p, for a unit-cell of a staggered array of cylinders as in Fig. 2. The quadratic form is occasionally discussed in the literature as part of the nonlinear corrections to Darcy's law (Mei and Auriault, 1991; Firdaouss et al., 1997). The regression, as detailed next, yields a very good fit for all regimes in the range $0 \le \mathrm{Re}_p \le \mathrm{Re}_{\mathrm{F2}}$, where $\mathrm{Re}_{\mathrm{F2}}$ is the pore Reynolds number assigned to the estimated end of the Forchheimer regime, see Khalifa et al. (2020).

$$\overline{G}(y) = \hat{c}_I(\epsilon(y)) + \hat{c}_{II}(\epsilon(y))\mathrm{Re}_p(y) + \hat{c}_{III}(\epsilon(y))\mathrm{Re}_p^2(y). \tag{17}$$

In Eq. (17), $\hat{c}_I(\epsilon(y))$, $\hat{c}_{II}(\epsilon(y))$ and $\hat{c}_{III}(\epsilon(y))$ are drag-related coefficients which depend on the porosity, and therefore, on the wall-normal coordinate y. We can reconstruct $\overline{G}$ from the data presented in Khalifa et al. (2020) considering the Darcy, transitional, and Forchheimer regimes.

Once $\overline{G}(y)$ is obtained, we can use it to define $\overline{f_{pd,i}}$ in Eq. (9). Denote $\partial\overline{\langle u_2'u_i'\rangle}/\partial y$ as $\overline{\mathcal{M}_{\mathcal{N},i}}$ to indicate that the Reynolds stress is an inherently nonlinear contribution to momentum. The desired form of the DANS equation is then obtained from substitution of Eqs. (13), (15), (17) and (16) in Eq. (9),

$$\begin{aligned}\overline{\mathcal{M}_{\mathcal{N},i}} = &-\zeta\delta_{i1} - \frac{1}{\rho}\frac{\partial\overline{\langle p\rangle}}{\partial y}\delta_{i2} + \nu\frac{\partial^2\overline{\langle u_i\rangle}}{\partial y^2} + \overline{\mathcal{I}_i} - \frac{\nu\epsilon N_T\pi D_\circ}{D_k^2 W}\hat{c}_I\,\overline{\langle u_i\rangle}\\ &- \frac{\epsilon N_T\pi D_\circ}{D_k W}\hat{c}_{II}\left\|\overline{\langle u_i\rangle}\right\|\overline{\langle u_i\rangle} - \frac{\epsilon N_T\pi D_\circ}{\nu W}\hat{c}_{III}\left\|\overline{\langle u_i\rangle}\right\|^2\overline{\langle u_i\rangle}.\end{aligned} \tag{18}$$

2.3. Permeability model

We omit the overline average notation $\overline{\cdot}$ from now on unless explicitly stated for simplicity. The nondimensional pressure gradient G and corresponding coefficients $\hat{c}_I$, $\hat{c}_{II}$ and $\hat{c}_{III}$ defining the permeability which should be used in Eq. (18), can be directly obtained from the data presented in Khalifa et al. (2020). The data for consideration is that corresponding to the piecewise approximations for the Darcy,

Table 1
Dimensionless coefficients for estimation of $G_{\text{piecewise}}$ taken from Khalifa et al. (2020).

ϵ	Re_T	Re_{F1}	Re_{TF}	G_0	γ_t	β	G_0^*
0.4	20.6	24.4	22.5	1350.0	0.163	7.0427	1274.057
0.5	12.4	17.27	14.835	340	0.0914	2.0361	329.909
0.6	9.39	10.7	10.045	111	0.0599	1.0402	106.5952
0.7	7.87	7.46	7.665	39.3	0.0492	0.7080	36.7638
0.8	7.08	2.15	4.615	13.1	0.0428	0.4207	12.0699
0.9	2.55	1.41	1.98	3.16	0.0514	0.2105	2.9446
1.0	0	0	0	0	–	0	0

Table 2
Dimensionless coefficients for G valid for Darcy, transitional, and Forchheimer regimes, see Eq. (17).

ϵ	$\hat{c}_I$	$\hat{c}_{II}$	$\hat{c}_{III}$
0.4	1321.8031	4.9033	2.097×10^{-2}
0.5	333.0872	1.8790	1.621×10^{-3}
0.6	107.9913	0.9729	6.868×10^{-4}
0.7	37.4884	0.6729	3.585×10^{-4}
0.8	12.2955	0.4097	1.133×10^{-4}
0.9	2.9731	0.2091	1.455×10^{-5}
1.0	0	0	0

transitional and Forchheimer regimes, in a staggered array of cylinders within a unit cell,

$$G_{\text{piecewise}} \equiv \begin{cases} G_0 + \gamma_t \text{Re}_p^2, & 0 \le \text{Re}_p \le \text{Re}_{\text{TF}}, \\ G_0^* + \beta \text{Re}_p, & \text{Re}_p \ge \text{Re}_{\text{TF}}. \end{cases} \tag{19}$$

We only consider the Darcy, transitional and Forchheimer regimes because this is a relatively simple parameterization of permeability in terms of a quadratic polynomial of Re_p, which also yields a reasonable representation of the porous flow. Cubic regressions of G in terms of Re_p such as those also published in Khalifa et al. (2020) have the inconvenience of potentially yielding negative values of G for some range of Re_p, which is undesirable for a roughness-drag model. In Eq. (19), G_0 is the nondimensional Darcy pressure gradient (G for $\text{Re}_p \to 0$), while β and γ_t are linear and quadratic coefficients for $G_{\text{piecewise}}$, respectively. Also, the intersection pore Reynolds number between the transitional and Forchheimer regimes, Re_{TF}, is obtained with the data from Khalifa et al. (2020) as $\text{Re}_{\text{TF}} = (\text{Re}_{\text{T}} + \text{Re}_{\text{F1}})/2$, where Re_{T} is the estimated Reynolds number at the end of the transition regime, and Re_{F1} is the estimated Reynolds number at the beginning of the Forchheimer regime. G_0^* is calculated by intersecting the transitional and Forchheimer regimes, such that $G_{\text{piecewise}}$ is continuous. The coefficients required for the estimation of $G_{\text{piecewise}}$ are taken from Khalifa et al. (2020), and are summarized in Table 1.

Once $G_{\text{piecewise}}$ is obtained, a linear least-squares fit is performed in order to obtain $\hat{c}_I$, $\hat{c}_{II}$ and $\hat{c}_{III}$ at every porosity value. This is reported in Table 2. Afterwards, $\hat{c}_I$, $\hat{c}_{II}$ and $\hat{c}_{III}$ can be interpolated for any value of ϵ (in the range $0.4 \le \epsilon \le 1$). Figs. 3(a) and 3(b) show $G_{\text{piecewise}}$ for the Darcy, transitional, and Forchheimer regimes, as defined in Khalifa et al. (2020), and the corresponding least-squares fit for porosity values $\epsilon = 0.6$ and $\epsilon = 0.9$. Note that the nonlinear vortex-shedding regime from Khalifa et al. (2020) is also shown in Figs. 3(a) and 3(b), although this regime is not included in the quadratic regression.

It is also necessary to comment on the procedure regarding the determination of the values and profiles N_T, $\epsilon(y)$, $D_\circ(y)$, and $D_k(y)$, which are necessary for the formulation of the drag forcing in Eq. (18). The suggested methodology for the determination of said values and profiles is discussed in Appendix A.

3. One-dimensional turbulence model formulation incorporating roughness parameterization

As written, Eq. (18) has a closure problem, i.e., the Reynolds stress $\overline{\mathcal{M}_{\mathcal{N},i}}$. The latter is responsible for turbulent dispersion as defined by Breugem (2005), or alternatively, turbulent advection. The closure for $\overline{\mathcal{M}_{\mathcal{N},i}}$ will be provided by the ODT model (Kerstein, 1999) as specified next.

ODT is best understood as a 1-D map-based model, in which an ensemble-average of stochastically sampled mapping implementations yields consistent turbulent fluxes, including scaling laws for turbulent transport, see Klein et al. (2022). The best application case for ODT is that of turbulent flows which exhibit statistics dominated by gradients in only one coordinate direction. This is usually the case for most boundary-layer flows, since wall-normal shear usually characterizes mean flow statistics to leading order. Following previous related applications of ODT for wall-bounded flows (Lignell et al., 2013; Freire and Chamecki, 2018; Klein et al., 2022), we utilize a so-called temporal ODT formulation, in which we time-advance scalar velocity component profiles on a wall-normal domain. The usual ODT governing equations for notional 1-D wall-normal scalar velocity profiles $u_i(y,t)$ can be written as

$$\frac{\partial u_i}{\partial t} + \mathcal{M}(u_i) = -\frac{1}{\rho}\frac{\mathrm{d}\overline{p}}{\mathrm{d}x}\delta_{i1} + \nu\frac{\partial^2 u_i}{\partial y^2} + f_{F,i\neq 2}. \tag{20}$$

Clearly, the scalar profiles $u_i(y,t)$ referenced in this section inherently fail to contain the same information as a 3-D DNS velocity field $u_i(x,y,z,t)$. For the temporal ODT formulation, the interest is instead on the statistical moments of $u_i(y,t)$, which should approximate those of the 3-D field in the limit of statistical stationarity, e.g., the wall-normal profile $\overline{u_i}$. In Eq. (20), $-\mathrm{d}\overline{p}/\mathrm{d}x > 0$ is a constant pressure-gradient forcing the flow, which corresponds to the time-averaged pressure gradient balancing the wall-shear stress in a wall-bounded configuration, e.g., a smooth-wall channel flow. Likewise, $f_{F,i\neq 2}$ is a body force, omitted for the wall-normal velocity component. Eq. (20) is integrated numerically in time with any numerical method of choice, however, $\mathcal{M}(u_i)$ is omitted from the numerical integration procedure. The latter is the model representation of the turbulent transport induced due to the advection of u_i by u_2. This assumes that wall-normal advection of the mean flow $\overline{u_i}$ by the mean velocity $\overline{u_2}$ is zero, as in usual boundary-layer assumptions on fully-developed flows with no-slip velocity conditions at the wall. In this context, if we denote $u_i(t_e, f(y))$ as a triplet map $f(y)$ on the 1-D profile $u_i(y)$, implemented at some (discrete) time t_e, then $\mathcal{M}(u_i)$ at a specific time t_e is, following (Kerstein et al., 2001),

$$\mathcal{M}(u_i,t)\delta(t-t_e): \quad u_i(t_e,y) \to u_i(t_e,f(y)) + c_i K(y). \tag{21}$$

In addition to triplet mapping the velocity profile, an additional modification due to a kernel function $K(y) = y - f(y)$ follows for a vector formulation of u_i (Kerstein et al., 2001). In this context, the kernel coefficient c_i (uniform in y) is related to an ODT model parameter α. This parameter, or more generally, α and $\alpha - 1$, can be loosely related to eigenvalues of the normalized anisotropy tensor. Thus, c_i loosely indicates how much kinetic energy is redistributed according to isotropy or anisotropy considerations during the transformation given by Eq. (21), also known as an eddy event in ODT (Kerstein et al., 2001). This links the effect by the kernel to the pressure-scrambling effect on incompressible flow. Note that we always use $\alpha = 2/3$. See also Appendix B for a derivation of the formula required for calculation of c_i, noting the dependence on α, and the inclusion of the body force effect.

On the assumption that $\overline{u_2} = 0$, it is understood that all effects contained in u_2 contribute only to turbulent transport, and not to mean advection. To that extent, the contribution of $f_{F,2}$ is omitted from Eq. (20), and considered instead as part of the energy redistribution due to the imposition of $c_i K$ during eddy events. For the case at discussion in this work, $f_{F,i}$ should be related to the drag forcing contribution. Some of the previous parametric forcing approaches for roughness drag used in DNS have omitted the use of the wall-normal ($i = 2$) drag forcing component from momentum equations, see Forooghi et al. (2018). There have also been ODT studies using parametric drag forcings, most notably in the context of canopy flows (Freire and Chamecki, 2018, 2021).

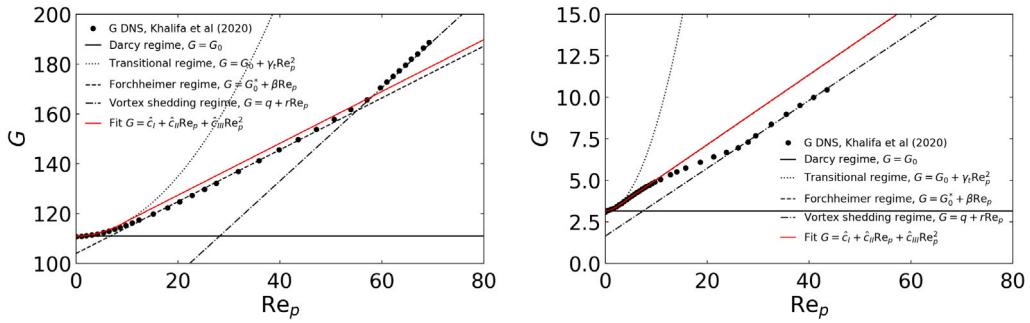

(a) $\epsilon = 0.6$ (b) $\epsilon = 0.9$

Fig. 3. Least-squares fit $G = \hat{c}_I + \hat{c}_{II}\mathrm{Re}_p + \hat{c}_{III}\mathrm{Re}_p^2$ from Eq. (17) and DNS-reported nondimensional pressure gradient G from Khalifa et al. (2020). The different regime approximations with reported values from Khalifa et al. (2020) are also shown in the figure (Darcy, Forchheimer, transitional, and vortex shedding regime).

Eddy events in ODT are sampled following a stochastic process, see details in Lignell et al. (2013). Sampled mappings are only implemented as long as the time-scale of the event, an eddy turnover time Δt_l, is feasible. Feasibility is decided for the rate $(\Delta t_l)^{-1}$, following a scaling proportional to the local kinetic energy (Kerstein et al., 2001; Klein et al., 2022),

$$\frac{1}{\Delta t_l} = \frac{C\nu}{l^2}\sqrt{\sum_i^3 \left(\frac{u_{i,K}\, l}{\nu}\right)^2 - Z}, \tag{22}$$

where l is the sampled length scale of the eddy event, and we have defined

$$u_{i,K} = \frac{1}{l^2}\int_l u_i(t, f(y))K(y)\,\mathrm{d}y. \tag{23}$$

We observe two terms within the square root in Eq. (22); the first one is the available kinetic energy within a candidate eddy event, while the second one is a viscous penalty-like term on said available kinetic energy. Empiricism is portrayed in ODT in the form of the model coefficients C and Z from Eq. (22), which relate to the frequency of implemented eddy events, and to a modeled viscous-suppression of very small eddies (due to TKE dissipation). Mappings are only implemented for sampled eddy events on which Δt_l is real, such that the quantity within the square-root in Eq. (22) is positive. We comment briefly on the effect of the C and Z model parameters for smooth-wall turbulent channel flows in Appendix C.

The ODT implementation for the double-averaged momentum equation, Eq. (18), time-advances scalar velocity component profiles until a statistically steady state. As in all ODT implementations to date, the time-(or ensemble-)average of the changes in the scalar profiles due to the stochastic implementation of eddy events, as per Eq. (21), results in the model representation of the Reynolds stress $\overline{\mathcal{M}_{N,i}}$, see also the appendices in Kerstein et al. (2001). The remaining conceptual difficulty concerning model implementation relates to the precise form of the governing equations for the time-dependent flow which must be numerically integrated in time within ODT. This need not be an issue, since the 3-D volume-averaged flow given by Eq. (5) can be time-advanced in the same way that a more traditional turbulent channel flow with smooth walls would be time-advanced in ODT using Eq. (20). The difference would only be related to the presence of the inhomogeneous momentum source or sink terms $\mathcal{I}_i$ and $f_{p,i}$. In this context, we need to omit the advection terms, as well as pressure gradient terms (other than uniform averaged source terms used to drive the mean flow) from Eq. (5). This is then entirely similar to the same way in which such terms are omitted in ODT smooth wall turbulent channel flow implementations (Lignell et al., 2013, 2018). As commented previously, we also omit the wall-normal component of the inhomogeneous terms, such that we take $\mathcal{I}_{i\neq 2}$ and $f_{p,i\neq 2}$. Consideration of $\mathcal{I}_{i\neq 2}$ also omits the pressure term from Eq. (6) in the inhomogeneous porosity term. There is an important issue which must be mentioned concerning the implementation of $f_{p,i\neq 2}$. Consider $\overline{f_{pd,i}}$ for the DANS momentum equation, Eq. (9), which should be given by $f_{p,i}$ in the volume-averaged Eq. (5). For $f_{p,i}$, we have the option to choose the same permeability modeling discussed in Section 2.2, but taking the time-dependent volume-average-related permeability $\mathcal{J}_{T,xx}$ instead of $\overline{\mathcal{J}_{T,xx}}$. This implies considering time-dependent G and $\langle u_i\rangle$ fields instead of their time-averaged versions $\overline{G}$ and $\overline{\langle u_i\rangle}$. This results in a time-averaged forcing which is not the same as that from Eq. (9). That is to say, $\overline{f_{p,i}} \neq \overline{f_{pd,i}}$, since the modeled time-dependent and subsequently averaged term $\overline{f_{p,i}}$ would involve averages of (velocity) products, which contrasts with the (directly) modeled DANS term $\overline{f_{pd,i}}$.

As one last remark, we note the calculation of the magnitude of the velocity vector for use in Eq. (16), i.e., $\|\langle u_i\rangle\|$, and subsequently in (17), in a similar fashion as Busse and Sandham (2012) and Forooghi et al. (2018). That is, we simply consider the magnitude of a corresponding velocity component $|\langle u_i\rangle|$ instead of the magnitude of the velocity vector. Denoting the equivalence of the (long-)time-averaged pressure gradient by $\rho\zeta \equiv \mathrm{d}\overline{p}/\mathrm{d}x < 0$, and the time-dependent equivalent of $\overline{\mathcal{M}_{\mathcal{N},i}}$ from Eq. (9) as $\mathcal{M}(\langle u_i\rangle)$, as to emphasize the application of Eq. (21) for eddy events, the ODT governing equation for use is then

$$\frac{\partial\langle u_i\rangle}{\partial t} + \mathcal{M}(\langle u_i\rangle) = -\frac{1}{\rho}\frac{\mathrm{d}\overline{p}}{\mathrm{d}x}\delta_{i1} + \nu\frac{\partial^2\langle u_i\rangle}{\partial y^2} + \mathcal{I}_i\delta_{i\neq 2} - \frac{\nu\epsilon N_T\pi D_\circ}{D_k^2 W}\hat{c}_I\langle u_i\rangle\delta_{i\neq 2} - \frac{\epsilon N_T\pi D_\circ}{D_k W}\hat{c}_{II}\,|\langle u_i\rangle|\,\langle u_i\rangle\delta_{i\neq 2} - \frac{\epsilon N_T\pi D_\circ}{\nu W}\hat{c}_{III}\langle u_i\rangle^3\delta_{i\neq 2}. \tag{24}$$

4. Limitations of the suggested modeling approach

In anticipation to the discussion of selected numerical results, we stress some issues of relevance concerning the limitations of our suggested model.

First and foremost, we note the use of a *standard* model for equivalent forcing of the hydrodynamic roughness effects as referenced by Aupoix (2015). In such *standard* models, mechanical dispersion is considered to be part of the corrections to Darcy's law. Arguably, our model may confound, to some extent, two different physical phenomena.

Second, the roughness-drag parameterization in Eq. (24) is solely made up of terms of the form $\mathrm{Re}_p^m\langle u_i\rangle\delta_{i\neq 2}$ (m being an integer, $m \leq 2$). All forcing terms, to that extent, represent drag contributions as in the PFA of Busse and Sandham (2012) and Forooghi et al. (2018). In drag dominated surfaces, or surfaces exhibiting large drag penalties, this is not an issue. We refer to the findings of Flack et al. (2020a,b), in which rough surfaces exhibiting positive skewness Sk are also those exhibiting the largest drag penalties. As in Busse and Sandham (2012) and Forooghi et al. (2018), it is also not possible to account for effects such as shielding or sheltering, which occur for very dense (d-type) roughness. Consensus on the effective criterion to distinguish

between sparse and dense roughness focuses on the effective slope ES, although there is no definite agreement on a threshold value of ES which would characterize said sparse-dense distinction or an associated transition. For the purpose of this work, we consider surfaces observing $ES < 0.35$ as of sparse roughness, while surfaces with larger effective slopes are considered in the dense roughness regime. The threshold value for ES follows the discussion in Chung et al. (2021) and Kadivar et al. (2021). As described so far, the best application cases for our model correspond to sparse (or k-type) roughness surfaces, which also exhibit positive skewness (peak-dominated sparse roughness surfaces with $ES < 0.35$ and $Sk > 0$). Roughness surfaces exhibiting negative skewness (pit-dominated surfaces), may be characterized by recirculation and separation effects within the roughness cavities (pits), see Jelly and Busse (2019). This cannot be captured with a drag model. A modified near-wall treatment for the mean streamwise flow in such cases is discussed in Section 6.2.

Although we apply our modeling approach to different roughness types, it is important to stress that some roughness types cannot be represented by discrete cylindrical elements. The use of a profile such as $D_\circ(y)$ in the parametric forcing, thus, may be ineffective. Another important issue is the case of a roughness described by an array of uniform cylindrical roughness elements, in which all of them observe the same cylindrical diameter D and roughness height k. In said case, $D_\circ(y)$ exhibits a discontinuity, since $D_\circ(y < k) = D$ and $D_\circ(y \geq k) = 0$, implying a discontinuous forcing term. This is not consistent with the continuous enhanced drag perceived by the flow for $y \geq k$ as commented in Chedevergne (2021). In Chedevergne (2021), this is corrected with a decaying exponential function which multiplies the original cylindrical drag coefficient. This could be interpreted as the application of a Brinkman correction to Darcy's law in order to properly match the roughness sublayer with the fluid layer above it, see also Chandesris and Jamet (2006). Unlike Chedevergne (2021), we do not foresee any additional treatment to that extent.

Further remarks derive from our pseudo-isotropic assumption for the permeability. We rely on the same relative strength (forcing coefficients) for streamwise and spanwise components of the roughness-drag forcing. We also use a similar drag form as a dissipation-like term affecting the kinetic energy redistribution during eddy events, see Appendix B. Mei and Auriault (1991) stress that permeability cannot be isotropic for finite Reynolds number effects, and Aupoix (2015) discusses how an anisotropic permeability with a distinctively different form for the wall-normal component of the roughness forcing could help toward better modeling of the contributions due to mechanical dispersion. Busse and Sandham (2012) also claim that different forcing forms for every momentum component, may lead to drag-reduction effects. Modifications to the ODT model parameter α, or the energy redistribution procedure during eddy events, could be beneficial in that sense. However, this is considered out of scope in the present work.

In general, the proposed modeling approach is focused on providing closure for the Reynolds shear stress with ODT, which can be achieved independently from the chosen parameterization of the roughness. In this context, additional limitations of the suggested modeling approach also relate to the usual limitations of the ODT model when simulating smooth-wall turbulent flow, see McDermott (2005), Lignell et al. (2013) and Klein et al. (2022).

5. Description of the study cases

Table 3 lists the study cases evaluated in this work, detailing both surface and flow features. Cases F-Ia and F-III correspond to surfaces with homogeneous and regular roughness, see Fig. 4. The cases F-Ia and F-III were originally evaluated in Forooghi et al. (2018), and are characterized by viscous-scaled average roughness heights $k^{+(\mathrm{MD})} = 67$ and $k^{+(\mathrm{MD})} = 110$, respectively, with the turbulent flow characterized by a friction Reynolds number $\mathrm{Re}_{\tau,\mathrm{MD}} \approx 500$. We note that case F-III is a surface in which all discrete roughness elements exhibit the same roughness height k (despite being dissimilarly distributed on the surface). Cases P-15/360 and P-60/360 correspond to surfaces with homogeneous and irregular roughness, see Fig. 5. The cases P-15/360 and P-60/360 were originally studied by Peeters and Sandham (2019), and are characterized by $k^{+(\mathrm{MD})} = 15$ and $k^{+(\mathrm{MD})} = 60$, respectively, with a turbulent flow at $\mathrm{Re}_{\tau,\mathrm{MD}} = 360$. We also perform, for reference, smooth-wall turbulent channel flow simulations at $\mathrm{Re}_\tau = 500$ (noted as case S-500) and $\mathrm{Re}_\tau = 360$ (noted as case S-360). Note that quantities $\{\cdot\}^+$ are defined in correspondence with the scales determining associated Reynolds numbers, such that $\{\cdot\}^+$, $\{\cdot\}^{+(\mathrm{MD})}$ and $\{\cdot\}^{+(\mathrm{ref})}$ correspond to quantities normalized according to the scales defining the friction Reynolds numbers Re_τ, $\mathrm{Re}_{\tau,\mathrm{MD}}$ and $\mathrm{Re}_{\tau,\mathrm{ref}}$, respectively. As an example, $u^{+(\mathrm{MD})} = \overline{\langle u \rangle}/u_{\tau,\mathrm{MD}}$. All of the before mentioned Reynolds numbers are defined next.

All cases were simulated in a (confined) channel flow-like setting of total height $2H$, see Fig. 6. The scales k_{MD} and k_{ref} in Fig. 6 correspond to virtual wall location choices. The friction Reynolds number for a smooth-wall turbulent channel is defined in the usual way, $\mathrm{Re}_\tau = u_\tau H/\nu$, where $u_\tau = \sqrt{\tau_w/\rho}$ is the friction velocity normalization scale defined by the (smooth) wall-shear stress. The smooth-wall vis-

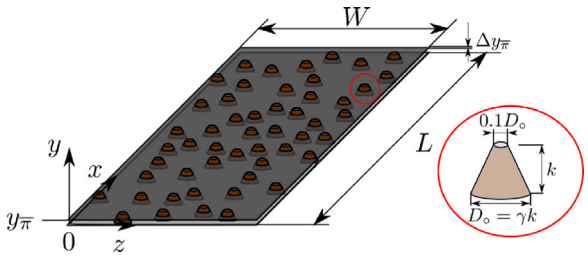

Fig. 4. Schematic visualization of the rough surfaces corresponding to cases F-Ia and F-III. The inset shows the form of the discrete roughness elements.

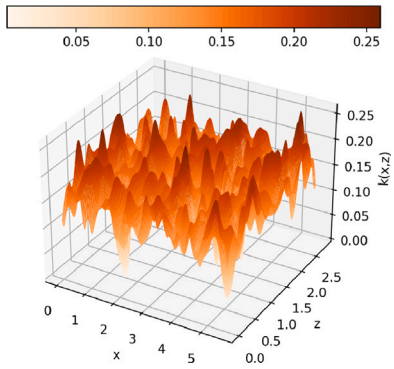

Fig. 5. Representative example of irregular rough surfaces (case P-60/360). Colors are associated with roughness height values.

Table 3
Study cases: surface and flow features. Symbol notation as follows: L surface length; W surface width; k average roughness height; k_{MD} meltdown roughness height; k_{RMS} root-mean-square roughness height; $k_{\max}$ roughness crest height; Sk normalized skewness (by k_{RMS}); ES effective slope; N_T number of roughness elements.

Parameter/case	F-Ia	F-III	P-15/360	P-60/360
L	$8H$	$8H$	$5.63\,(H - k_{\mathrm{MD}})$	$5.63\,(H - k_{\mathrm{MD}})$
W	$4H$	$4H$	$2.815\,(H - k_{\mathrm{MD}})$	$2.815\,(H - k_{\mathrm{MD}})$
k	$0.12H$	$0.19H$	$1/24\,(H - k_{\mathrm{MD}})$	$1/6\,(H - k_{\mathrm{MD}})$
k_{MD}	$0.074H$	$0.1H$	$0.04\,(H - k_{\mathrm{MD}})$	$0.16\,(H - k_{\mathrm{MD}})$
k_{RMS}	$0.045H$	$0.045H$	$0.0089\,(H - k_{\mathrm{MD}})$	$0.0358\,(H - k_{\mathrm{MD}})$
$k_{\max}$	$0.21H$	$0.19H$	$0.0653\,(H - k_{\mathrm{MD}})$	$0.2619\,(H - k_{\mathrm{MD}})$
Sk	0.21	0.21	−0.52	−0.52
ES	0.88	0.88	0.23	0.23
$\epsilon(y = 0)$	0.0455	0	0	0
N_T	645	1080	Profile $N_T(y)$	Profile $N_T(y)$

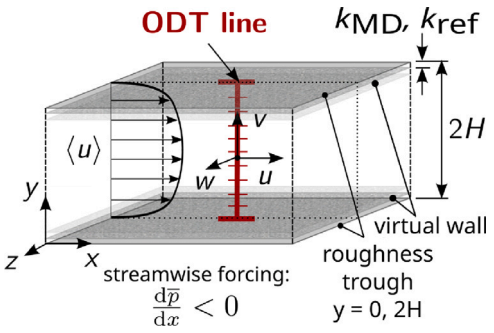

Fig. 6. Flow configuration sketch.

cous normalization scale is then $\delta_\nu = \nu/u_\tau$. The input friction Reynolds number $\mathrm{Re}_{\tau,\mathrm{MD}}$ for the rough wall channels is defined with the help of an *a priori* specified virtual wall location and a corresponding effective channel height,

$$\mathrm{Re}_{\tau,\mathrm{MD}} = \frac{u_{\tau,\mathrm{MD}}\left(H - k_{\mathrm{MD}}\right)}{\nu}. \tag{25}$$

Here, k_{MD} is the meltdown roughness height, an *a priori* estimate for the virtual wall location mainly based on geometric considerations, see Chan-Braun et al. (2011). We reserve the notation k_{ref} for an *a posteriori* estimation of the virtual wall, see also Chan-Braun et al. (2011). The input friction velocity $u_{\tau,\mathrm{MD}}$ is defined in terms of the fixed pressure gradient (FPG) driving the flow, with denoted equivalence $\rho\zeta \equiv \mathrm{d}\overline{p}/\mathrm{d}x$. The latter equilibrates the total stress at $y = k_{\mathrm{MD}}$, as per the integration from $y = k_{\mathrm{MD}}$ to $y = H$ of the time-averaged version of the streamwise component of Eq. (24),

$$\frac{\mathrm{d}\overline{p}}{\mathrm{d}x}\left(H - k_{\mathrm{MD}}\right) = \left[\tau_{\mathrm{tot},21}(y = H) - \tau_{\mathrm{tot},21}(y = k_{\mathrm{MD}})\right]. \tag{26}$$

We define the total shear stress $\tau_{\mathrm{tot},21}$ acting on a wall-parallel plane, in direction x_1 as

$$\tau_{\mathrm{tot},21}(y) = -\rho\overline{\langle u_2' u_1'\rangle} + \mu\frac{\partial\overline{\langle u_1\rangle}}{\partial y} - \rho\int_{y^*=y}^{y^*=H}\overline{f_{p,1}}\,\mathrm{d}y^* - \rho\int_{y^*=y}^{y^*=H}\overline{I_1}\,\mathrm{d}y^*. \tag{27}$$

Due to symmetry of the profile around $y = H$, we set $\tau_{\mathrm{tot},21}(y = H)$ to zero. Using $\tau_{\mathrm{tot},21}(y = k_{\mathrm{MD}})$ as a reference shear stress and Eq. (26), we define $u_{\tau,\mathrm{MD}}$ as

$$u_{\tau,\mathrm{MD}} = \sqrt{-\frac{1}{\rho}\frac{\mathrm{d}\overline{p}}{\mathrm{d}x}\left(H - k_{\mathrm{MD}}\right)}. \tag{28}$$

Usually, either $\mathrm{d}\overline{p}/\mathrm{d}x$ or $u_{\tau,\mathrm{MD}}$ are set for the simulation, in order to force a target $\mathrm{Re}_{\tau,\mathrm{MD}}$. The specification of $\mathrm{Re}_{\tau,\mathrm{MD}}$ is completed by specifying either the fluid properties (that is, a value of ν), the height H, or the effective height $H - k_{\mathrm{MD}}$. If ν is specified, then H or $H - k_{\mathrm{MD}}$ can be determined based on the specification of k_{MD}/H (or $k_{\mathrm{MD}}/(H - k_{\mathrm{MD}})$ as in Table 3), and vice versa. The consistency of the simulation can be verified by recalculation of $\mathrm{d}\overline{p}/\mathrm{d}x$ or $u_{\tau,\mathrm{MD}}$ using the mean flow statistics resulting from the simulation, i.e., Eqs. (26) and (27). The general use of Eq. (26) for calculation of the total shear stress at any y corresponds to the method of extrapolation from the centerline, see also a detailed discussion in Chan-Braun et al. (2011). Note that the input viscous length-scale for the rough-wall cases is defined as $\delta_{\nu,\mathrm{MD}} = \nu/u_{\tau,\mathrm{MD}}$.

For smooth-wall channel flow simulations, we resort to the use of no-slip boundary conditions at the walls, as well as uniform initial conditions. In the roughness wall simulations, we also use uniform initial conditions, but we enforce artificial no-slip conditions on the velocity at $y = k_{\mathrm{MD}}$, as per the effective virtual wall, see also the discussion on the wall-offset in Chung et al. (2021). In this way, all velocity values for $y \le k_{\mathrm{MD}}$ are set to zero during the ODT deterministic time integration. Notwithstanding the imposition of the artificial boundary conditions, eddy events are allowed to map regions of the velocity profile all the way down to $y = 0$.

We note that $k_{\mathrm{MD}} \approx k$ for cases P-15/360 and P-60/360. We also note the different input length scale normalizations for the numerical domain dimensions, L and W, the average roughness height k, the meltdown roughness height k_{MD}, and others, in the published studies of Forooghi et al. (2018) and Peeters and Sandham (2019). For consistency with said studies, we list in Table 3 the dimensional form of L, W, k, and others, indicating the corresponding normalization scale used in Forooghi et al. (2018) (the full channel height, H) and Peeters and Sandham (2019) (the effective or hydraulic channel height, $H - k_{\mathrm{MD}}$), as appropriate.

Figs. 7(a), 7(c) and 7(e) show the viscous-scaled obtained drag forcing coefficients for surface cases F-Ia and F-III. Likewise, Figs. 7(b), 7(d) and 7(f) show the drag coefficients for surface cases P-15/360 and P-60/360. The viscous-scaled coefficients, using $u_{\tau,\mathrm{MD}}$ and the viscous length scale $\nu/u_{\tau,\mathrm{MD}}$ as normalization scales, are noted as $C_I^{+(\mathrm{MD})}$, $C_{II}^{+(\mathrm{MD})}$ and $C_{III}^{+(\mathrm{MD})}$. According to Eq. (24), these are

$$\begin{aligned} C_I^{+(\mathrm{MD})} &= \frac{\left(H - k_{\mathrm{MD}}\right)^2}{\mathrm{Re}_{\tau,\mathrm{MD}}\nu}\left(\frac{\nu\epsilon N_T \pi D_\circ}{D_k^2 W}\hat{c}_I\right), \\ C_{II}^{+(\mathrm{MD})} &= \left(H - k_{\mathrm{MD}}\right)\left(\frac{\epsilon N_T \pi D_\circ}{D_k W}\hat{c}_{II}\right), \\ C_{III}^{+(\mathrm{MD})} &= \mathrm{Re}_{\tau,\mathrm{MD}}\nu\left(\frac{\epsilon N_T \pi D_\circ}{\nu W}\hat{c}_{III}\right). \end{aligned} \tag{29}$$

Unlike our suggested deterministic method to estimate the drag forcing coefficients $C_I^{+(\mathrm{MD})}$, $C_{II}^{+(\mathrm{MD})}$ and $C_{III}^{+(\mathrm{MD})}$ (see also Appendix A), Forooghi et al. (2018) suggest an ad-hoc estimation of the drag forcing coefficients based solely on dimensional grounds. We refer to the method from Forooghi et al. (2018) as an ad-hoc PFA for roughness forcing, noting that such method does not make use of inhomogeneous porosity terms. The corresponding forcing coefficients from Forooghi et al. (2018) are noted for distinction as $C_{IF}^{+(\mathrm{MD})}$, $C_{IIF}^{+(\mathrm{MD})}$ and $C_{IIIF}^{+(\mathrm{MD})}$,

$$C_{IF}^{+(\mathrm{MD})} = \frac{H^2}{\mathrm{Re}_{\tau,\mathrm{MD}}}\frac{k_K s}{\epsilon^3}, \qquad C_{IIF}^{+(\mathrm{MD})} = \frac{1}{2}c_D s_f H, \qquad C_{IIIF}^{+(\mathrm{MD})} = 0. \tag{30}$$

The variables ϵ, s and s_f are supplied input profiles of porosity, interface area per unit volume, and projected frontal surface area per unit volume, respectively, which can be directly obtained from a given surface $\widetilde{k}(x,z)$. Nonetheless, k_K and c_D are two model constants, a Carman-Kozeny constant and a drag coefficient, which have no modeling guideline, and can only be calibrated *a posteriori*. That is, these are two tunable model coefficients. This is different to our suggested model, which has no tunable coefficients for drag parameterization. To that extent, the only model coefficients correspond to those in the ODT model. This is a relevant advantage of the presented framework in comparison to that of Forooghi et al. (2018), or to other previous ad-hoc parameterizations (Busse and Sandham, 2012). Figs. 7(a), 7(c) and 7(e) show the comparison of the coefficients $C_{IF}^{+(\mathrm{MD})}$, $C_{IIF}^{+(\mathrm{MD})}$ and $C_{IIIF}^{+(\mathrm{MD})}$ from Forooghi et al. (2018) with our suggested VAT-based framework. It is seen that the Darcy coefficient $C_I^{+(\mathrm{MD})}$ is smaller in the VAT-framework, but is compensated by a larger $C_{II}^{+(\mathrm{MD})}$ Forchheimer coefficient in all cases. The $C_{III}^{+(\mathrm{MD})}$ coefficient is not considered in Forooghi et al. (2018). Said coefficient is also of a very small magnitude in our suggested VAT-based framework. For the regular roughness surfaces, Figs. 7(a), 7(c) and 7(e) show that the drag coefficients exhibit a monotonic behavior for $y > k_{\mathrm{MD}}$, and retain a constant value for $y \le k_{\mathrm{MD}}$. The constant value is in fact irrelevant, given the imposition of the artificial no-slip conditions.

Finally, we stress the very different type of surfaces evaluated in this work. On one hand, cases F-Ia and F-III exhibit positive skewness, $Sk > 0$. These are drag-dominated surfaces, which corresponds to the range of applicability of our model. However, these cases observe regular roughness exhibiting an effective slope $ES = 0.88$, see Forooghi et al. (2018). This is a significantly larger value in comparison to our

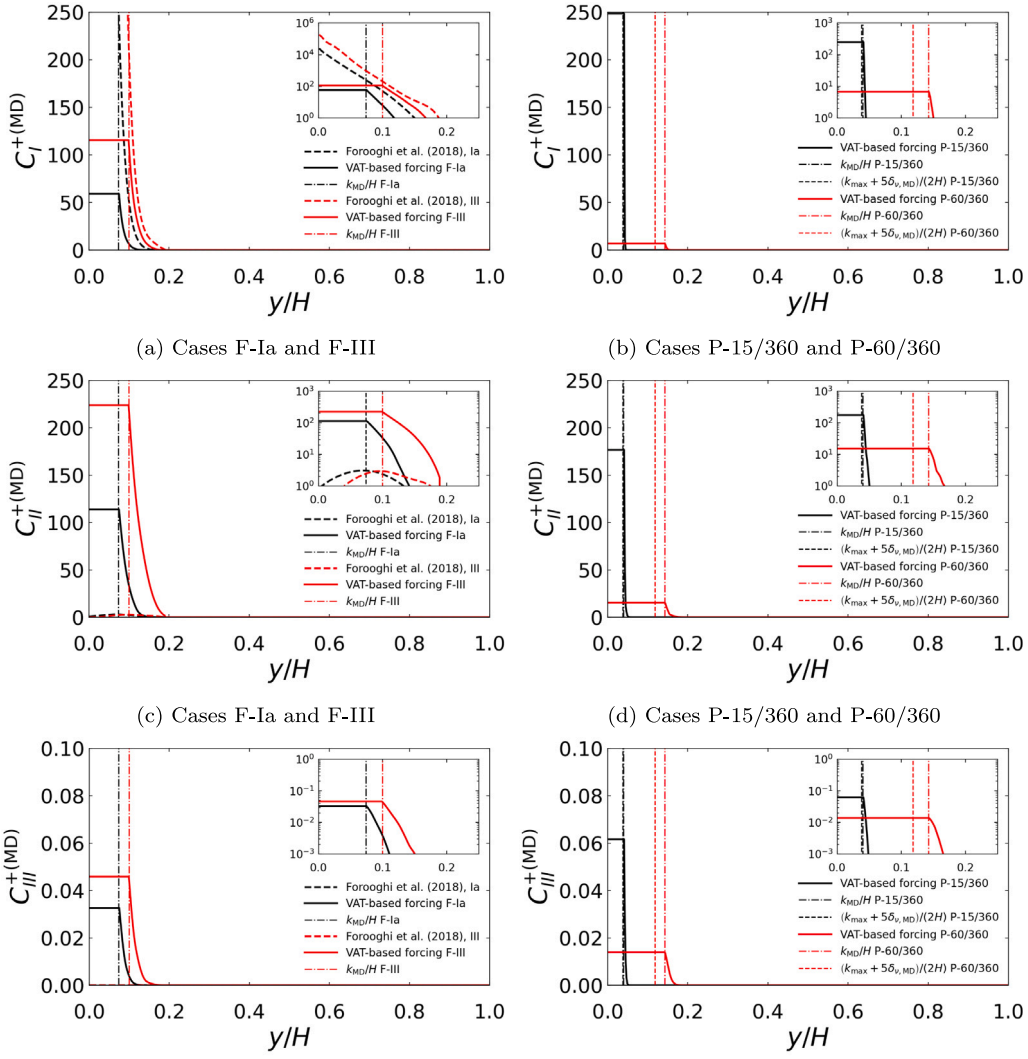

(a) Cases F-Ia and F-III

(b) Cases P-15/360 and P-60/360

(c) Cases F-Ia and F-III

(d) Cases P-15/360 and P-60/360

(e) Cases F-Ia and F-III

(f) Cases P-15/360 and P-60/360

Fig. 7. Drag forcing coefficients and location of the *a priori* virtual wall (vertical dotted-dashed line). The insets within the plots show a logarithmic scale of the vertical axis. In (a), (c) and (e), we show a comparison with the ad-hoc coefficients from Forooghi et al. (2018). In addition to the position of the *a priori* virtual wall, (b), (d) and (f) also show the location of the center of a modeled large-scale cavity vortex (vertical dashed lines, see Section 6.2).

assumed threshold of 0.35 defining *wavy* or sparse roughness surfaces, see also Chung et al. (2021) and Kadivar et al. (2021). Hence, cases F-Ia and F-III are assumed as surfaces corresponding to the dense roughness regime (d-type roughness), for which we expect some shortcomings from our model application, see Section 4. On the other hand, cases P-15/360 and P-60/360, which correspond to irregular roughness surfaces, exhibit an effective slope $ES = 0.23$. Said surfaces are considered *wavy* or sparse roughness surfaces. Although no shielding or sheltering effects should be present in this type of surfaces, we note that cases P-15/360 and P-60/360 also exhibit negative skewness, $Sk < 0$ (pit-dominated roughness surface (Flack et al., 2020a,b)). The latter makes P-15/360 and P-60/360 ill-candidates for our model application. We discuss a way to remediate some of the shortcomings for these surfaces in Section 6.

5.1. Choice of the ODT model parameters

We comment now on the choice of the ODT model parameters required for the simulations. These are specified in Table 4. We choose *a priori* values of Z based on theoretical justifications, partially motivated by the smooth-wall choice for Z. The latter is proportional to the location of the maximum TKE production and mostly insensitive to Re_τ in smooth-wall flow, see Appendix C.

We simulate ODT equations with the presence of roughness-drag forcing terms, and both with and without the inhomogeneous porosity term $\mathcal{I}_i$, see Eq. (24). For ODT simulations considering $\mathcal{I}_i = 0$ (that is, without the inhomogeneous porosity term), we find that a good estimate for $\sqrt{Z}$ is the distance $k_{\max} - k_{\mathrm{MD}}$ in viscous units, multiplied by a factor which ranges between 1 and 5/3. The distance $(k_{\max} - k_{\mathrm{MD}})^{+(\mathrm{MD})}$ is considered to be the viscous coordinate of the TKE production peak $y_{\hat{P}}^{+(\mathrm{MD})}$, measured from the *a priori* virtual wall (mainly geometric-based choice) at $y = k_{\mathrm{MD}}$. This is motivated by the findings of authors who have noted that the peak of TKE production in rough wall flow is usually close, although generally not equal, to the position of the roughness crest, see Yuan and Piomelli (2014). The factor ranging between 1 and 5/3 follows the observation that the peak production to dissipation ratio is $\hat{P}/D_{\hat{P}} \approx 5/3$ in smooth wall channels (Lee and Moser, 2015), while in a fully rough flow it is closer to 1 (Yuan and Piomelli, 2014). For ODT simulations considering the inhomogeneous porosity term, we find that a good estimate for $\sqrt{Z}$ is given by the smallest of the distances between $(k_{\max} - k_{\mathrm{MD}})^{+(\mathrm{MD})}$ and the location of the maximum of the Reynolds shear stress $y^+_{\max,\mathrm{RSS}}$ in smooth-wall flow, multiplied by a factor which ranges between 1 and 5/3. The coordinate

Table 4
ODT model parameters for turbulent flow simulations.

Parameter/case	C	Z
S-500	6.5	400
F-Ia (ad-hoc PFA forcing)	3.5	5350
F-Ia (VAT-based forcing with $\mathcal{I}_i = 0$)	3.5	5350
F-Ia (VAT-based forcing including $\mathcal{I}_i$)	6.5	1250
F-III (ad-hoc PFA forcing)	2	2500
F-III (VAT-based forcing with $\mathcal{I}_i = 0$)	2	2500
F-III (VAT-based forcing including $\mathcal{I}_i$)	4	1250
S-360	6.3	400
P-15/360 (VAT-based forcing with $\mathcal{I}_i = 0$)	7	400
P-15/360 (VAT-based forcing including $\mathcal{I}_i$)	7	400
P-60/360 (VAT-based forcing with $\mathcal{I}_i = 0$)	6	1550
P-60/360 (VAT-based forcing including $\mathcal{I}_i$)	6	1200

$y^+_{\mathrm{max,RSS}}$ can be calculated *a priori* as $\sqrt{\mathrm{Re}_\tau/\kappa}$, being $\kappa \approx 0.4$ an estimate for the von Kármán constant, see Lee and Moser (2015).

Model parameters listed in Table 4 evidence that there is a small sensitivity to C in smooth-wall flow, which appears when simulating with ODT at relatively low Re_τ. In smooth-wall flow, the parameter C is calibrated in order to match the (global) skin friction value C_f, see details in Appendix C. The values of C listed in Table 4 for all rough wall cases are calibrated values obtained for a reasonable overall match of the mean velocity profile when compared with reference data. The calibration procedure in the rough wall cases, however, did not specifically match the C_f value of the flow. Unlike in smooth-wall flow, there are more length-scales involved for flows over rough walls, which may lead to the situation in which only matching C_f leads to worse overall matching of the mean profile. In general, ODT simulations omitting implementation of the inhomogeneous porosity term observe smaller C values in order to match the required skin friction value. Conversely, C values for ODT simulations implementing $\mathcal{I}_i$ are closer to the corresponding smooth-wall flow simulation values. Constancy of C at asymptotically large Re_τ is expected in any case. Since the evaluated Re_τ (or alternatively $\mathrm{Re}_{\tau,\mathrm{MD}}$) in all study cases is relatively low, we expect some variability of C.

6. Turbulent flow simulation results

Fig. 8 shows a spatial visualization of the turbulent channel flow. The figure is a spatio-temporal visualization of the velocity field within the ODT domain, indicating the position of sampled ODT eddy events. Note that the horizontal axis also shows the equivalent streamwise advancement given by the transformation $\Delta x = \int U_b \mathrm{d}t$, where U_b is the resulting bulk flow velocity. Figs. 8(a) and 8(b) show a typical ODT run for a smooth wall turbulent channel flow at $\mathrm{Re}_\tau = 500$ and $\mathrm{Re}_\tau = 360$, cases S-500 and S-360, respectively. Conversely, Figs. 8(c) and 8(e), show the same turbulent flow at $\mathrm{Re}_\tau = 500$, with rough surface cases F-Ia and F-III. Likewise, Figs. 8(d) and 8(f), show the turbulent flow at $\mathrm{Re}_\tau = 360$, with rough surface cases P-15/360 and P-60/360. Besides the naturally larger eddy activity at $\mathrm{Re}_\tau = 500$ in comparison to $\mathrm{Re}_\tau = 360$, we note the overall absence of eddy events in the rough wall simulations below the *a priori* virtual wall location. We stress that the eddy events in ODT are not necessarily related to physical eddies in a turbulent flow. The eddy events are simply a model representation of turbulent advection events, which determine the Reynolds shear stress after ensemble-averaging. For comparison with DNS data, it is therefore better to refer directly to the Reynolds shear stress, which we will do later. In smooth-wall flow, ODT eddy events are smaller, in average, since they are mostly located near the smooth-wall. In the roughness wall simulations, we notice larger eddy events. This may come as a result of mainly two factors. The first one relates to the chosen values of the ODT model parameter Z, which is larger than in the smooth wall cases (except for case P-15/360 which uses the same smooth wall value). The parameter Z effectively suppresses eddies below a certain size (Kerstein et al., 2001), implying larger eddies overall in the roughness flow simulations. The second factor relates to the drag forcing, which, in general, reduces the magnitude of the velocity field, and thus reduces gradients near the virtual wall. Alternatively, the below-virtual-wall treatment may forbid implementation of eddy events entirely, e.g., due to imposed artificial boundary conditions.

Table 5
Average roughness height, input (*a priori*) friction Reynolds number and virtual wall location, and *a posteriori* estimation of the virtual wall location and corresponding friction Reynolds number. All listed cases correspond to ODT simulations using the VAT-based forcing implementation, considering all terms of Eq. (24).

Parameter/case	F-Ia	F-III	P-15/360	P-60/360
$\mathrm{Re}_{\tau,\mathrm{MD}}$	498	499	360	360
$k^{+(\mathrm{MD})}$	67	110	15	60
$k^{+(\mathrm{MD})}_{\mathrm{MD}}$	≈40	≈55.4	≈15	≈60
k/H	0.1200	0.1900	0.0400	0.1429
k_{MD}/H	0.074	0.1	≈0.04	≈0.1429
k_{ref}/H	0.1178	0.1512	0.0414	0.1548
$\mathrm{Re}_{\tau,\mathrm{ref}}$	≈468	≈460	≈373	≈354

Roughness wall simulation results can lead to the estimation of a different, *a posteriori* estimation of the virtual wall at $y = k_{\mathrm{ref}}$. The *a posteriori* estimation is calculated with the centroid of the (streamwise) roughness-drag forcing profile $\overline{f_{p,1}}$, see Chan-Braun et al. (2011) and Jackson (1981),

$$k_{\mathrm{ref}} = \frac{\int_0^H y\overline{f_{p,1}}\,\mathrm{d}y}{\int_0^H \overline{f_{p,1}}\,\mathrm{d}y}. \tag{31}$$

The definition of the *a posteriori* virtual wall location implies that a different Reynolds number, $\mathrm{Re}_{\tau,\mathrm{ref}}$, can be obtained as a result of the simulation, using the effective height $H - k_{\mathrm{ref}}$, and the *a posteriori* friction velocity $u_{\tau,\mathrm{ref}} = \sqrt{\tau_{\mathrm{tot},21}(k_{\mathrm{ref}})/\rho}$. That is,

$$\mathrm{Re}_{\tau,\mathrm{ref}} = \frac{u_{\tau,\mathrm{ref}}\left(H - k_{\mathrm{ref}}\right)}{\nu}. \tag{32}$$

Fig. 9 shows the forcing profiles for each study case, where $\overline{f_{p,x}}$ is determined from a steady-state balance of the momentum equation, Eq. (24). Table 5 lists the obtained *a priori* and *a posteriori* virtual wall locations and Reynolds numbers.

6.1. Peak-dominated, dense roughness cases

Fig. 10 shows a comparison of the mean velocity profile obtained for the regular, peak-dominated roughness cases F-Ia and F-III. The agreement for case F-Ia is quite reasonable in what seems to be a logarithmic layer of the flow. Deviations with respect to reference DNS data are always observed in the roughness sublayer of the flow profile. For case F-III, the model results are far from optimal, especially if $\mathcal{I}_i$ is omitted from Eq. (24). The shortcomings in the results obtained for case F-III were already foreseen in Section 4, mainly due to the regular form of the roughness elements. That is, all roughness elements in this case observe the same diameter and average roughness height, thus causing a nonphysical discontinuous forcing around $y = k$. This issue, together with missing sheltering effects characteristic of surfaces observing $Sk > 0$, leads to the violation of several model assumptions.

Fig. 11 shows the mean velocity profiles after shifting due to the virtual wall offset, using both the *a priori* and *a posteriori* estimations of the virtual wall locations, as well as the corresponding scalings derived from it. It is clear that the use of a different virtual wall location would lead to a different estimation of the slope of the logarithmic layer, i.e., a different value of the von Kármán constant, and correspondingly, a different estimation of the roughness function. We do not discuss the log-layer quantitatively any further. A discussion on the roughness function is deferred to Section 6.3.

We remark that Fig. 10 shows the resulting mean velocity profiles which are obtained when using the drag forcing coefficients $C^{+(\mathrm{MD})}_{IF}$,

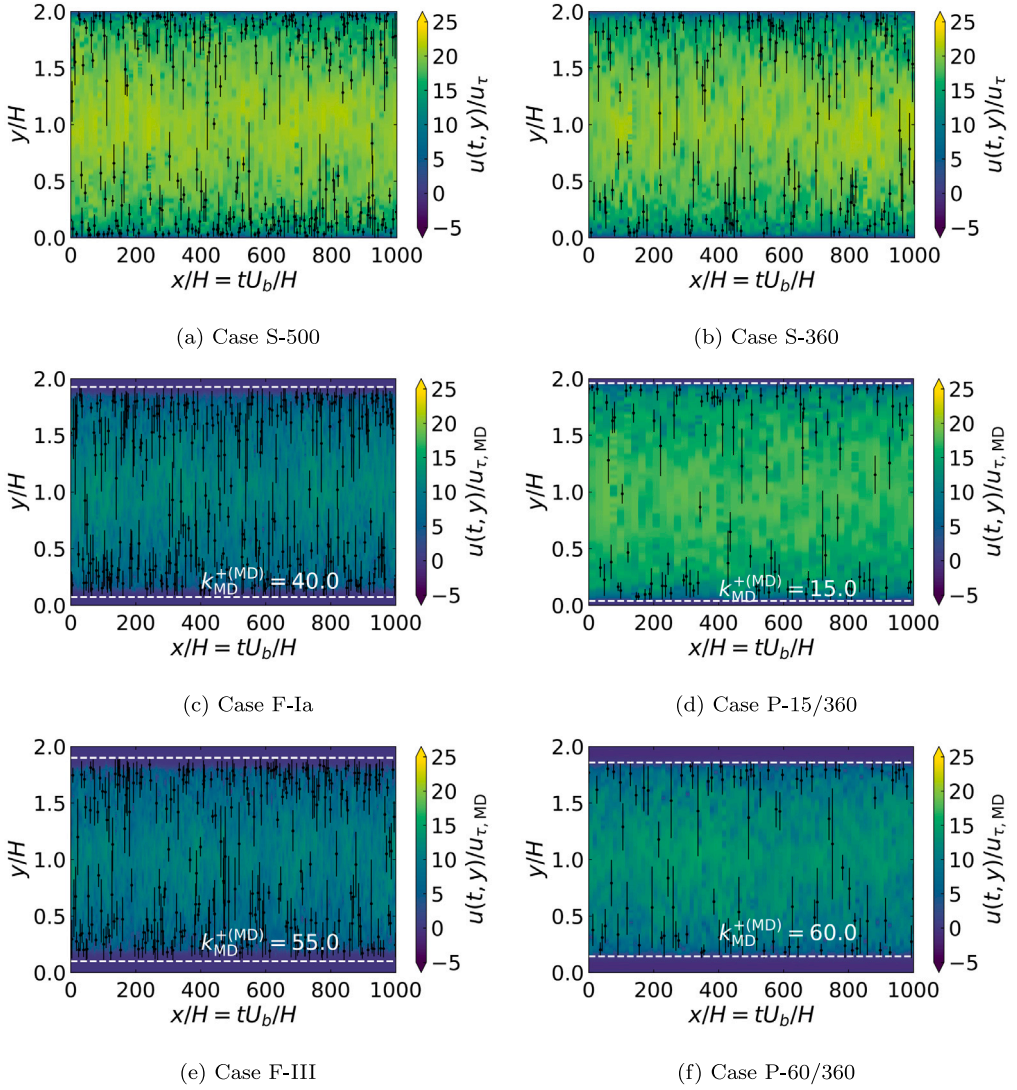

(a) Case S-500 (b) Case S-360

(c) Case F-Ia (d) Case P-15/360

(e) Case F-III (f) Case P-60/360

Fig. 8. Spatio-temporal visualization of ODT velocity fields indicating position of eddy events (a small cross indicates the center of the eddy event transformation, while the error bar indicates the size of the event). Only one out of every 10 eddy events is shown for clarity. The position of the *a priori* virtual wall $k_{\mathrm{MD}}^{+(\mathrm{MD})}$ is also indicated. Visualizations corresponding to simulations of rough surfaces correspond to ODT simulations implementing all VAT-based forcing terms from Eq. (24).

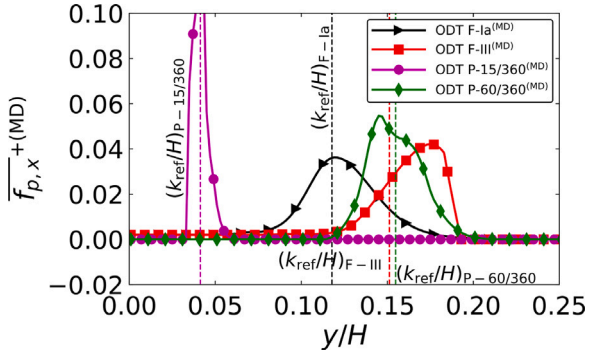

Fig. 9. ODT wall-normal streamwise drag forcing profiles $\overline{f_{p,x}}$ obtained for VAT-based forcing implementation, considering all terms of Eq. (24). The estimated value of k_{ref} per Eq. (31) is also shown as a vertical dashed line.

$C_{IIF}^{+(\mathrm{MD})}$ and $C_{IIIF}^{+(\mathrm{MD})}$ from Forooghi et al. (2018) (ad-hoc PFA roughness forcing), and the drag coefficients obtained using the VAT framework presented here, both considering and omitting implementation of the $\mathcal{I}_i$ term in Eq. (24). For consistency with the way in which the ad-hoc PFA is used in the DNS of Forooghi et al. (2018), no virtual wall treatment is used in the simulations using said ad-hoc forcing coefficients. That is, the no-slip condition is applied at $y = 0$. It is remarkable to note that the mean velocity profile obtained by both PFA and VAT-based forcing methods omitting implementation of $\mathcal{I}_i$ is almost identical (using the same ODT model parameters). One may argue that the predicted log-layer slope is overpredicted in these simulations, and that deviations are observed in the outer layer of the flow profile when comparing to reference DNS data. The largest deviations with respect to DNS data are observed in the fully rough case F-III with $k^{+(\mathrm{MD})} = 110$, in the lower part of the roughness sublayer of the flow. Although the roughness sublayer agreement in both cases F-Ia and F-III is far from optimal when compared with DNS data, there is also disagreement between DNS results for the roughness sublayer from Forooghi et al. (2018). This concerns DNS results obtained when using either the PFA or the incorporation of the roughness topology with immersed boundaries. Differences between ODT and DNS predictions could be mostly attributed to the overall form of the chosen forcing parameterization as discussed in Section 4. The differences also evidence, naturally,

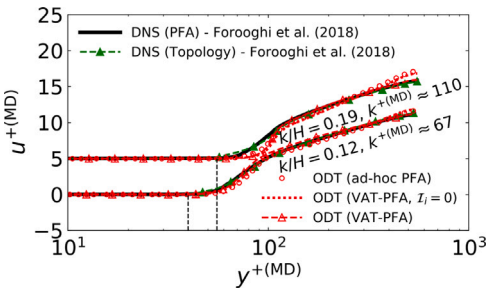

Fig. 10. Mean velocity profile for cases F-Ia and F-III. ODT results are shown using both the ad-hoc forcing for drag suggested in Forooghi et al. (2018) (ad-hoc PFA), as well as the VAT motivated forcing (VAT-PFA), including and omitting implementation of $\mathcal{I}_i$. Reference DNS results from Forooghi et al. (2018) are shown as well, for both ad-hoc forcing (PFA), and full roughness topology simulations (Topology). Results for case F-III have been shifted 5 units upward for better visualization. Vertical dashed lines indicate the position $k_{\mathrm{MD}}^{+(\mathrm{MD})}$.

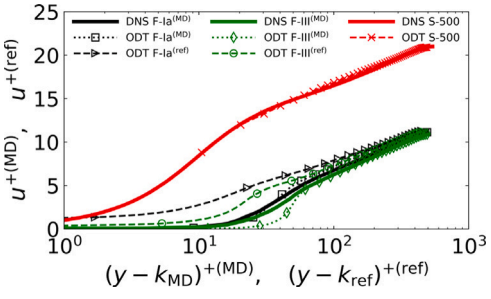

Fig. 11. Comparison of mean velocity profiles for cases S-500, F-Ia, and F-III, utilizing both *a priori* (k_{MD}) and *a posteriori* (k_{ref}) virtual wall locations and scalings. Cases F-Ia, and F-III correspond to simulations using the VAT-derived forcing (including implementation of $\mathcal{I}_i$). DNS data from Lee and Moser (2015) at $\mathrm{Re}_\tau = 550$ is shown as a reference for case S-500, while DNS data (PFA) from Forooghi et al. (2018) is shown as reference for cases F-Ia and F-III.

that ODT does not behave in the same way as DNS when using the same forcing. An additional remark in this context is that, although not noticeable in Fig. 10, cases F-Ia and F-III observe a region near the wall, below k_{MD}, which exhibits negative velocity values of very small magnitude, see the DNS results obtained using the full roughness topology with immersed boundaries in Forooghi et al. (2018). This would correspond to the shielding or sheltering effects, which are not allowed in our model by construction. The PFA approach in Forooghi et al. (2018) is also not able to reproduce these effects. Overall, neither the PFA approach in Forooghi et al. (2018) nor the present approach are able to accurately predict the drag throughout the entire roughness sublayer for dense (d-type) roughness.

Figs. 12(a) and 12(b) show the stress contributions for cases F-Ia and F-III, respectively, when using all terms implied by the VAT-based forcing. A linear extrapolation of the total stress from $y = H$ (outer layer) all the way to the wall at $y = 0$ is also shown. As commented in Chan-Braun et al. (2011), the extrapolation of the total stress to the *a priori* estimation of the virtual wall location (k_{MD}) is consistent with the steady-state balance of the integrated momentum equation, see Eq. (26). Note that the integrated drag forcing shown in Figs. 12(a) and 12(b) is calculated in two ways. The first one, $\int \overline{f_{p,x,\mathrm{dir}}}\mathrm{d}y$, corresponds to a direct estimation based on the (time-)averaged forcing terms from Eq. (24). The second one, $\int \overline{f_{p,x,\mathrm{bal}}}\mathrm{d}y$ corresponds to the steady-state balance of the momentum equation, as per Eq. (26). As expected, both calculation methods coincide for $y \geq k_{\mathrm{MD}}$.

The TKE production scaled in viscous units is also overlayed in Figs. 12(a) and 12(b) to show that the peak of production $\hat{P}$ generally coincides with a peak in the viscous stress. It is also seen that $\hat{P}$ approximately coincides with the position of the average roughness height k in case F-III, i.e., the uniform roughness height of all roughness elements in said case. Also visible in Figs. 12(a) and 12(b) is the Reynolds shear stress and the mean viscous stress. We note that the start of $\overline{\langle u'v' \rangle}$ is slightly delayed in comparison to the DNS PFA prediction. Simultaneously, as seen in Fig. 10, the start of the mean velocity profile is delayed in comparison to the DNS prediction. Since the near-virtual-wall region is dominated by the drag forcing contribution, differences in the Reynolds shear stress can be directly attributable to the chosen form of the roughness forcing. Concerning the role of the inhomogeneous porosity term in the double-averaged momentum balance, it is seen that its influence is relatively small when compared to the forcing term. Nonetheless, this term mostly affects the region near the virtual wall, and hence, has a non-negligible effect in the form of the mean velocity profile, as evidenced in Fig. 10.

Figs. 13(a) and 13(b) show the Reynolds stress components (normal stresses and shear stress $\overline{\langle u'v' \rangle}$). Here, the difference between ad-hoc and VAT forcings is more noticeable in the roughness sublayer prior to the peak of $\overline{\langle u'u' \rangle}$ and $\overline{\langle v'v' \rangle}$. The obtained normal stresses $\overline{\langle v'v' \rangle}$ and $\overline{\langle w'w' \rangle}$ are different, despite observing the same initialization, which contrasts with smooth-wall ODT flow (Lignell et al., 2013, 2018). This is due to the presence of the drag forcing in the spanwise momentum equation, and its omission for the wall-normal momentum equation in Eq. (24). The normal Reynolds stress $\overline{\langle v'v' \rangle}$ also exhibits close to peak values at the *a priori* virtual wall location when the ad-hoc forcing is used. These are inconsistent physics which signalize the importance of the VAT-based framework in ODT. This is also evidence that the DNS-used PFA forcing from Forooghi et al. (2018) naturally does not behave in the same way in our 1-D framework if applied directly without modifications. The Reynolds shear stress $\overline{\langle u'v' \rangle}$ shows no sensitivity to the type of forcing used (ad-hoc or VAT-based), but it is certainly affected by the omission or implementation of the $\mathcal{I}_i$ term. Although agreement of the Reynolds shear stress seems to be very accurate in Fig. 13(a), we note that small deviations for said Reynolds stress are present within the roughness sublayer. Nonetheless, we argue that, overall, there is a reasonable prediction of the Reynolds shear stress when compared to the reference DNS data, which signalizes the reliability of the ODT model to represent turbulent dispersion. For the normal Reynolds stress components, the deviation is significantly larger in comparison to DNS data. In particular, $\overline{\langle u'u' \rangle}$ is significantly overpredicted beyond the roughness sublayer when the inhomogeneous porosity term is omitted. A better representation is obtained by including said term $\mathcal{I}_i$. The spanwise normal Reynolds stress $\overline{\langle w'w' \rangle}$ is better represented than the wall-normal stress $\overline{\langle v'v' \rangle}$ when $\mathcal{I}_i$ is omitted, although the position of the peak in the latter one is not correctly predicted. In general, the model faces difficulties in the representation of normal Reynolds stress components, which is known from smooth-wall ODT flows, e.g., see Klein et al. (2022). Some interesting analogies may be drawn from this, in the sense that the model performance is somehow similar to the way in which the Boussinesq hypothesis holds for RANS turbulence. That is, the model is able to successfully predict the Reynolds shear stress, since the mean shear is more or less reasonably predicted. However, it struggles to predict the normal components of the Reynolds stress (the TKE), for which an additional transport equation is also required in linear eddy viscosity turbulence models.

6.2. Pit-dominated, sparse roughness cases

Cases F-Ia and F-III correspond to drag dominated surfaces due to their highly positive skewness values ($Sk > 0$, peak-dominated roughness). In contrast, cases P-15/360 and P-60/360 correspond to negatively skewed surfaces ($Sk < 0$, pit-dominated roughness). As presented so far, and noting the discussion in Section 4, our modeling approach is not suitable for negatively skewed surfaces due to

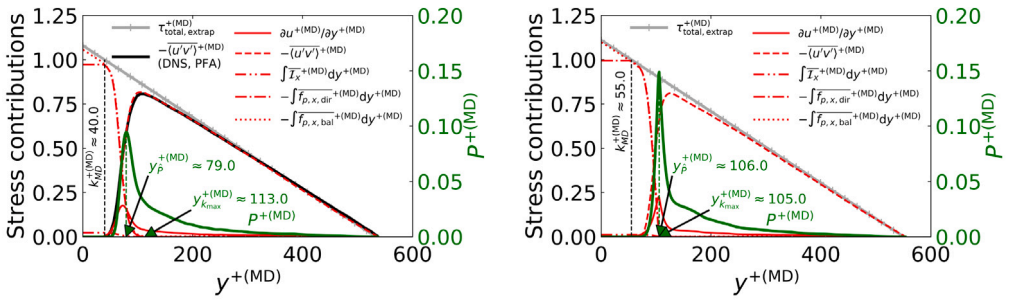

(a) Case F-Ia (VAT-PFA) (b) Case F-III (VAT-PFA)

Fig. 12. Stress contributions obtained with ODT comprising the mean viscous stress $\partial u^{+(MD)}/\partial y^{+(MD)}$, the Reynolds shear stress $\overline{\langle u'v' \rangle}^{+(MD)}$, the integral of the time-averaged inhomogeneous porosity term, and of the time-averaged drag forcing term, as well as the linear extrapolation of the total stress from the outer layer to the wall. The ODT obtained TKE production $P^{+(MD)}$ (green, right vertical axis) is also overlayed on the figure. Reference DNS data from Forooghi et al. (2018) is shown for reference. Vertical dashed lines show the position of k_{MD} and of the peak of TKE production $y_{\hat{P}}$.

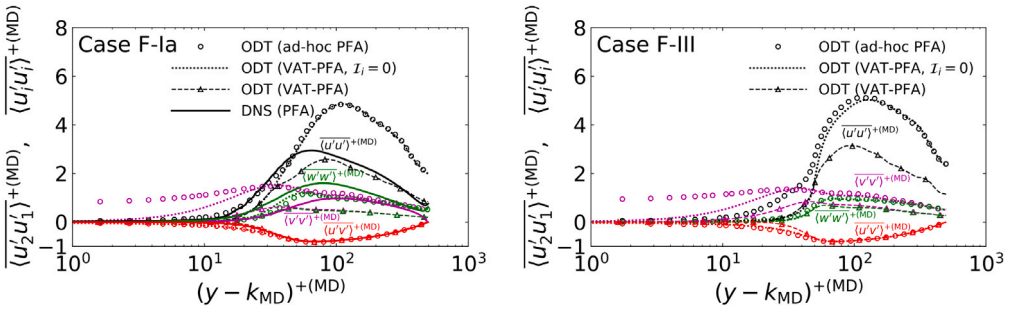

(a) Case F-Ia (b) Case F-III

Fig. 13. Wall-normal profiles of the Reynolds stress components (normal stresses and crosswise shear stress) obtained with ODT. Colors correspond to different Reynolds stress components. Reference DNS from Forooghi et al. (2018) is shown as reference for case F-Ia (no reference DNS data was available for case F-III). (For interpretation of the references to color in this figure legend, the reader is referred to the web version of this article.)

local drag reduction, flow recirculation and separation in the near-wall roughness cavities, see also Jelly and Busse (2019). As a way to remediate the shortcoming, at least in terms of the mean flow, we suggest a near-wall modified treatment for the mean flow within the cavities, which aims to emulate the flow due to a large-scale vortex. The size of the largest vortex within the cavities is $k_{max} - 5\delta_{\nu,MD}$, since k_{max} is the maximum roughness height, and $5\delta_{\nu,MD}$ is the generally accepted extent of the viscous sublayer, being $\delta_{\nu,MD} = \nu/u_{\tau,MD}$ the input viscous length scale. The center of the large-scale vortex is located at $y = (k_{max} + 5\delta_{\nu,MD})/2$, measured from the roughness trough (i.e., $y = k_{min} = 0$). As in the drag-dominated surfaces, we observe continuous drag-forcing (and FPG application) until the meltdown roughness height $y = k_{MD}$. Crosswise and spanwise components are set to zero as in the artificial boundary condition treatment of drag-dominated surfaces for $y \leq k_{MD}$. However, we do not impose any artificial boundary condition for the streamwise velocity. Instead, we maintain uniform forcing coefficients, as well as the flow-driving FPG, if applicable, until the center of the hypothesized large-scale vortex, since this range still corresponds to positive streamwise mean flow within the roughness cavities ($\langle \overline{u} \rangle > 0$ above the vortex center for any $y \geq (k_{max} + 5\delta_{\nu,MD})/2$). In the range $0 \leq y < (k_{max} + 5\delta_{\nu,MD})/2$, we drive the streamwise velocity component with a reversed FPG, and omit any form of forcing. The adverse pressure gradient below the vortex center, which has the same magnitude as the flow-driving FPG but with reversed sign, induces negative flow velocities. We also forbid the mapping of profiles below the large-scale vortex center, $y < (k_{max} + 5\delta_{\nu,MD})/2$, on the justification that it is physically not reasonable to expect that the effects of free stream eddies penetrate into the recirculation cavities.

Figs. 14 and 15 show the mean velocity profiles for cases P-15/360 and P-60/360, with and without virtual wall offsets, respectively. The offset in Fig. 15 considers both the *a priori* and the *a posteriori* estimation of the virtual wall location and its derived scalings. For the negatively skewed roughness surfaces, the LVM leads unmistakeably to better results using the same VAT drag forcing and ODT model parameters C and Z. Note that the results shown in Figs. 14 and 15 correspond to the implementation of all terms derived for the VAT-based forcing, i.e., including the term $\mathcal{I}_i$. The flow patterns motivating the LVM treatment are best visualized by the near-wall negative velocity zone of case P-60/360 in Fig. 14. It is not possible to obtain a reasonable matching of the mean velocity profiles without using LVM, regardless of the choice of ODT model parameters C or Z. The parametric drag forcing has only a damping effect on the velocity, such that it is unable to induce negative flow velocities. Hence, the need for the adverse pressure gradient below the vortex center.

We note that the bulk flow velocity is slightly overestimated in cases P-15/360 and P-60/360. This contrasts with the underestimation of U_b seen for cases F-Ia and F-III. Case P-15/360 is almost hydrodynamically smooth, and uses essentially the same ODT model parameter values C and Z as the smooth-wall reference case, see Table 4. The overestimation of the bulk flow velocity (underestimation of C_f) in case P-15/360, and also in case P-60/360, corresponds to the expected behavior of the ODT model for small roughness amplitudes (or small roughness forcing magnitudes), i.e., on the approximate absence of drag forcing. The underestimation of U_b seen for cases F-Ia and F-III can, in turn, be explained on the basis of the drag forcing parameterization. The forcing exhibits significantly larger magnitudes for the positively skewed cases F-Ia and F-III. Therefore, said forcing mostly determines

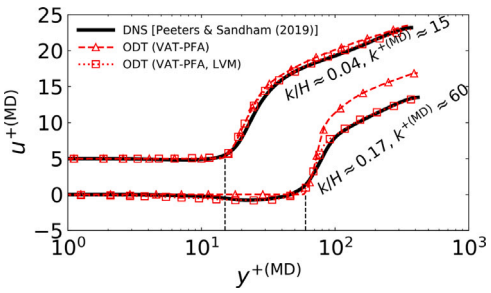

Fig. 14. Mean velocity profile in viscous units for cases P-15/360 and P-60/360. ODT results are shown for both the near-wall artificial boundary condition treatment, and the near-wall large-scale cavity vortex model (labeled as LVM). DNS results from Peeters and Sandham (2019) are shown for reference. Results for case P-15/360 have been shifted 5 units upward for better visualization. Vertical dashed lines indicate the position $k_{\mathrm{MD}}^{+(\mathrm{MD})}$.

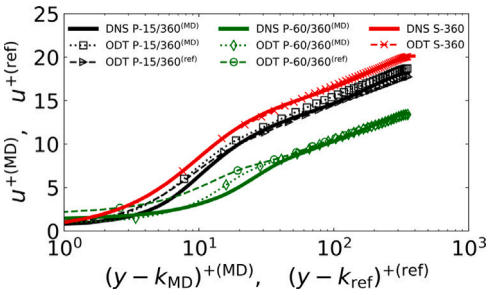

Fig. 15. Comparison of mean velocity profiles for cases S-360, P-15/360, and P-60/360, utilizing both *a priori* (k_{MD}) and *a posteriori* (k_{ref}) virtual wall locations and scalings. Presented cases P-15/360 and P-60/360 utilize the near-wall LVM treatment. DNS data from Moser et al. (1999) at $\mathrm{Re}_\tau = 395$ is shown as a reference for case S-360, while DNS data from Peeters and Sandham (2019) is shown as reference for cases P-15/360, and P-60/360.

U_b (or alternatively C_f), unlike the ODT model parameter-dominated smooth-wall and negatively-skewed-roughness flow C_f, see also Figs. 7(a), 7(c), 7(b) and 7(d).

Figs. 16(a) and 16(b) show the Reynolds stress components (normal stresses and shear stress $\overline{\langle u'v' \rangle}$). As in the mean velocity, the difference due to the LVM treatment is more readily noticeable for case P-60/360. It is interesting that case P-15/360 (with or without LVM), as well as the LVM omission in case P-60/360 yield the double peak of the normal Reynolds stress profile $\overline{\langle u'u' \rangle}$ which is characteristic from smooth wall ODT simulations (Lignell et al., 2013, 2018). For case P-15/360, which is almost hydrodynamically smooth, $\overline{\langle u'u' \rangle}$ profiles are underpredicted, which is typical for ODT. Conversely, case P-60/360 shows increased values of $\overline{\langle u'u' \rangle}$. Specifically, ODT results considering the LVM treatment seem to match better the DNS data by partially eroding one of the peaks in the wall-normal profile of $\overline{\langle u'u' \rangle}$. Notwithstanding the representation of $\overline{\langle u'u' \rangle}$, there is a striking similarity of the normal Reynolds stress components $\overline{\langle v'v' \rangle}$ and $\overline{\langle v'v' \rangle}$ predicted by ODT in cases P-15/360 and P-60/360. As commented before, these cases are more heavily dominated by the usual ODT dynamics in comparison to the drag-dominated surfaces of cases F-Ia and F-III. This explains why the behavior of $\overline{\langle v'v' \rangle}$ and $\overline{\langle u'w' \rangle}$ in both negatively skewed surface cases is similar to that of smooth wall flow. The Reynolds shear stress $\overline{\langle u'v' \rangle}$ exhibits sensitivity to the LVM use or omission in case P-60/360, which is expected from the different mean velocity profiles associated to said case. Arguably, a better matching is obtained when using the LVM treatment.

6.3. Evaluation of the roughness function

The study cases presented in Section 5 correspond to a range of low-to-moderate (input) friction Reynolds numbers. As it is well known from smooth-wall turbulent channel flows, it is only possible to obtain a well-defined logarithmic layer for large friction Reynolds number flows, see Lee and Moser (2015). This is an inconvenience for the evaluation of the roughness function ΔU^+. Another issue of relevance for the determination of ΔU^+ are the seemingly different log-layer slopes (i.e., von Kármán constant) obtained with ODT in Sections 6.1 and 6.2. In order to avoid inconsistent measurements, we resort to a simplified evaluation of ΔU^+ by the difference between the centerline velocities between smooth-wall and rough-wall channel flow profiles. This is the same treatment applied in Busse and Sandham (2012), Busse et al. (2017) and Thakkar et al. (2017). That is, we evaluate the roughness function utilizing the *a priori* or *a posteriori* virtual wall-related friction velocity normalization as

$$\Delta U^{+(\mathrm{MD,ref})} = u^+_{\mathrm{smooth}}(y/H = 1) - u^{+(\mathrm{MD,ref})}_{\mathrm{rough}}(y/H = 1), \tag{33}$$

where the superindex $\{\cdot\}^{+(\mathrm{MD,ref})}$ indicates the choice of either $u_{\tau,\mathrm{MD}}$ or $u_{\tau,\mathrm{ref}}$ as the corresponding normalization scales.

Fig. 17 shows the obtained roughness function $\Delta U^{+(\mathrm{MD,ref})}$ calculated as per Eq. (33), using either the *a priori* or the *a posteriori* virtual wall location and scalings. Notably, the suggested model framework delivers roughness function values which are in reasonable agreement with DNS data.

7. Summary and conclusions

We presented the application of a high-fidelity stochastic one-dimensional modeling approach to turbulent channel flows with homogeneous roughness. In order to be able to represent the roughness in a 1-D rationale, we formulated a parametric forcing approach for the roughness-induced drag using VAT. This is different from previous ad-hoc forcing approaches for DNS (Busse and Sandham, 2012; Forooghi et al., 2018), and more similar to DANS approaches using discrete roughness element methods (Chedevergne, 2021). Present ODT model results evidence the important role of the inhomogeneous porosity term omitted in the previous ad-hoc forcing approaches. Additionally, there is an inherent limitation in said ad-hoc PFAs, since they introduce arbitrary coefficients which must be calibrated *a posteriori*. This is indeed the case of the ad-hoc PFA from Forooghi et al. (2018), in which two parameter coefficients related to the Carman-Kozeny constant and an additional arbitrary drag coefficient, k_K and c_D, were calibrated with DNS. For the purpose of modeling, this is unjustifiably expensive in terms of computational resources. Our alternative forcing approach, in turn, utilizes VAT and identifies correspondences with nondimensional drag representations for staggered cylinder arrays, which have been extensively studied in the past (e.g., see Khalifa et al. (2020)). For the representation of the turbulent flow, we rely on a stochastic map-based turbulence model, which is not exempt from empiricism. From this point of view, ODT introduces model parameters which must be calibrated. We argue that for the case at discussion, there is only one model parameter necessitating calibration in ODT, the C parameter. Overall, this model with one free parameter is an improvement from the previous ad-hoc PFA in Forooghi et al. (2018) with two different model parameters.

The main goal of our ODT implementation is focused on providing closure for the Reynolds shear stress, i.e., the turbulent dispersion in a volume-averaged flow over homogeneous roughness. The present model has some important limitations concerning our assumed form for the permeability of the roughness. This includes, but is not limited to, the potential misrepresentation of mechanical dispersion as drag, the inability to model shielding or sheltering effects in dense roughness, among others. These limitations are similar to those associated with any

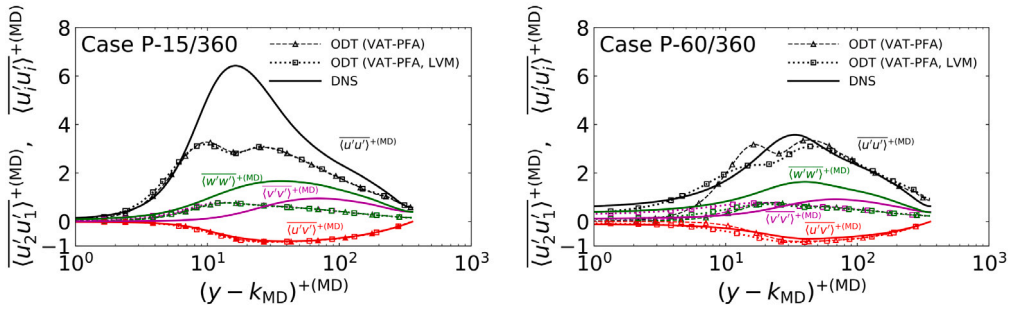

(a) Case P-15/360 (b) Case P-60/360

Fig. 16. Wall-normal profiles of the Reynolds stress components (normal stresses and crosswise shear stress) obtained with ODT. Colors correspond to different Reynolds stress components. In (a), ODT results for $\langle v'v'\rangle$ and $\langle w'w'\rangle$ overlap completely. DNS data from Peeters and Sandham (2019) is shown for reference.

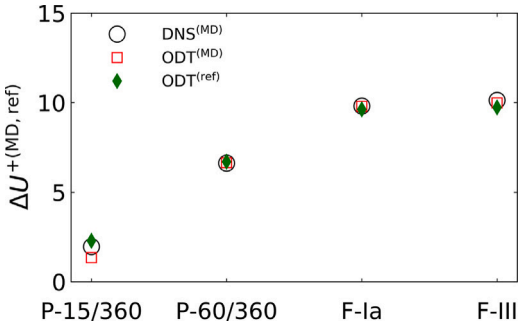

Fig. 17. Roughness function values obtained for each case using all terms in the ODT implementation of Eq. (24) related to the VAT-based forcing. Case results P-15/360 and P-60/360 correspond to simulations using the near-wall LVM treatment. Case results F-Ia and F-III correspond to simulations using the VAT-based forcing (VAT-PFA). DNS reference data is taken from Forooghi et al. (2018) and Peeters and Sandham (2019).

DANS or RANS approach using non-optimal drag forcing parameterizations. The advantage here being that, regardless of the chosen forcing parameterization, ODT observes a more robust physically-based, dynamical model formulation based on less model parameters when compared to alternative filter-based approaches, e.g., $\mathcal{K}-\omega$ RANS models. This is because neither assumptions on the form of laws of the wall, nor of the form of blending functions for consistency between different mean flow layers, nor for damping functions for asymptotic consistency of near-wall mean flow behavior, are required. The business case of the present model is, therefore, sustained on the grounds of providing an economical framework to evaluate turbulent channel flows over rough walls, doing so with full-scale resolution of the turbulent flow, thus offering extended predictive capabilities in comparison to filter-based models.

We have verified that the suggested VAT-based forcing is able to deliver physically compatible results in the dimensionally reduced framework of the ODT model. The 1-D model is an economical numerical tool that has the capability to provide a reasonably accurate predictor of the roughness function. The behavior of the model, as well as the involved model assumptions, differ between positively-skewed (drag-dominated) surfaces and negatively-skewed surfaces. Although the Reynolds shear stress is reasonably predicted in all cases, the model fails to adequately predict normal Reynolds stresses such as $\langle u'u'\rangle$, as well as some features of the mean velocity profile within the roughness sublayer.

Future work should be devoted to the improvement of the drag forcing parameterization observing the limitations of the model stressed in Section 4. A more extensive parametric study for different types of roughness, as well as a wider range of Reynolds number for evaluation of the turbulent flow, could also be envisaged.

CRediT authorship contribution statement

Juan A. Medina Méndez: Writing – review & editing, Writing – original draft, Visualization, Validation, Software, Methodology, Investigation, Formal analysis, Data curation, Conceptualization. **Marten Klein:** Writing – review & editing, Supervision, Conceptualization. **Jurriaan W.R. Peeters:** Writing – review & editing, Data curation. **Heiko Schmidt:** Writing – review & editing, Supervision, Resources, Funding acquisition.

Declaration of competing interest

The authors declare that they have no known competing financial interests or personal relationships that could have appeared to influence the work reported in this paper.

Acknowledgments

We gratefully acknowledge the invitation for submission of this work extended by both the editorial board and the organizing committee of the 13th Turbulence and Shear Flow Symposium (TSFP13). Likewise, we would like to extend a special acknowledgment to Pourya Forooghi, who greatly collaborated with the initial momentum of this research through fruitful discussions. Furthermore, we profoundly acknowledge the observations, comments and contributions to this work made by all reviewers during the peer review process of the manuscript. Marten Klein and Heiko Schmidt also acknowledge the support by the German Federal Government, the Federal Ministry of Research, Technology and Space, and the State of Brandenburg, within the framework of the joint project EIZ: Energy Innovation Center (project numbers 85056897 and 03SF0693A) with funds from the Structural Development Act (Strukturstärkungsgesetz) for coal-mining regions. Finally, we also acknowledge the support of the BTU Graduate Research School in the form of Conference Travel Grants, for allowing participation in TSFP13.

Appendix A. Determination of wall-normal roughness profiles for surface parameterization

A.1. Generalized method

We discuss next the method for characterization of the wall-normal roughness surface profiles required for characterization of G, or of the drag-forcing term $f_{p,i}$. This method is applied in general when the roughness surface topology $\widetilde{k}(x,z)$ is available. We have applied this method for the surfaces exhibiting homogeneous and irregular roughness, i.e., cases P-15/360 and P-60/360, since $\widetilde{k}(x,z)$ was available. The discussion is specialized for said cases. One surface example is shown in Fig. 5. The average roughness height k for the before mentioned surfaces is considered to be the mean-peak-to-valley height in a 5×5 tiling, see Thakkar et al. (2017). With the surface configuration detailed in Peeters and Sandham (2019), the estimation of k approximates the meltdown roughness height k_{MD}, if the tiled surface is discretized with equidistant spacings for the purpose of the evaluation of k_{MD},

$$k_{\mathrm{MD}} = \frac{1}{LW}\int_0^L \int_0^W \widetilde{k}\,\mathrm{d}z\mathrm{d}x. \tag{A.1}$$

The wall-normal origin ($y = 0$) is set at the lowest point of the surface such that $k_{\mathrm{min}} = 0$ and $\epsilon(y=0) = 0$, while k_{max} is the highest surface coordinate $\widetilde{k}_{\mathrm{max}}(x,z)$. Other quantities such as k_{MD}, k_{RMS} and Sk can be directly computed from the surface $\widetilde{k}(x,z)$, as in Eq. (A.1).

Wall-normal profiles of the area occupied by the roughness $A_{\circ}(y)$ and of the free (fluid-occupied) area $A_k(y)$, are determined as follows. The surface $\widetilde{k}(x,z)$ is discretized in a number of levels $M = \mathrm{Re}_{\tau,\mathrm{MD}}$, which is the wall-normal resolution of the numerical simulation. At each wall-normal coordinate y^m, with $0 \le m \le M$, we use the simple thresholding routine (*threshold*) of the open source Python computer vision library OpenCV, in order to binary split the regions at the coordinate y^m which are inside and outside of the roughness surface $\widetilde{k}(x,z)$. This yields $N_T(y^m)$ regions (or contours) of roughness-equivalent area, as well as $N_k(y^m)$ regions of fluid-equivalent area. OpenCV is able to compute the total area of the $N_T(y^m)$ and $N_k(y^m)$ contours, such that it is possible to estimate $A_{\circ}(y)$ and $A_k(y)$, respectively. Note that $A_{\circ}(y) + A_k(y) = LW$. The porosity is then estimated in a straightforward fashion according to Eq. (2) as

$$\epsilon(y) = \frac{1}{LW}\int_0^L \int_0^W \chi(x,y,z)\,\mathrm{d}z\mathrm{d}x = 1 - \frac{A_{\circ}(y)}{LW}. \tag{A.2}$$

The roughness element-equivalent and pore-equivalent diameters, $D_{\circ}$ and D_k, respectively, are calculated as

$$D_{\circ}(y) = \sqrt{\frac{4A_{\circ}(y)}{\pi N_T(y)}}, \qquad D_k(y) = \sqrt{\frac{4A_k(y)}{\pi N_k(y)}}. \tag{A.3}$$

Fig. A.18(a) shows the determined porosity profiles for the cases with irregular roughness. Fig. A.18(b) shows the determined equivalent diameter profiles for said cases.

A.2. Reconstruction of a surface using statistical moments of the roughness distribution

We comment now on cases in which the roughness surface topology $\widetilde{k}(x,z)$ is not available, but several of the statistical area-moments of the roughness distribution are known instead. This was the case for surfaces F-Ia and F-III from Forooghi et al. (2018). In order to obtain the values and profiles N_T, $\epsilon(y)$, $D_{\circ}(y)$, and $D_k(y)$, we resorted to a virtual reconstruction of an abstract rough surface using statistical moments of the roughness. To that extent, we consider discrete distributed roughness elements as shown schematically in Fig. 4. We note that the type of surfaces for which the following methodology applies is precisely that shown in Fig. 4, characterized by a peak-dominated roughness with $Sk > 0$.

The first-order statistical area-moment of $\widetilde{k}(x,z)$ is the meltdown roughness height k_{MD}, which is defined by Eq. (A.1). The root-mean-square value k_{RMS} is the second-order moment of the deviation (with respect to the mean k_{MD}), and is calculated in a similar way, as well as the normalized skewness Sk (third-order moment). A detailed discussion can be found in Forooghi et al. (2017). By specifying k_{MD}, k_{RMS} and Sk, it is possible to fit a probability density function (PDF) of the area-moments of $\widetilde{k}(x,z)$. We choose to fit a Weibull PDF $\mathcal{W}(\widetilde{k};\phi,\theta)$, following the suggestions by Yang et al. (2022). We use ϕ and θ as shape and scale parameters of the PDF, respectively, such that

$$\mathcal{W}(\widetilde{k};\phi,\theta) = \phi\theta^{\phi}\widetilde{k}^{\phi-1}e^{-\left(\theta\widetilde{k}\right)^{\phi}}. \tag{A.4}$$

The cumulative distribution function (CDF) associated to $\mathcal{W}(\widetilde{k};\phi,\theta)$ (noting that $\mathcal{W}(\widetilde{k};\phi,\theta)$ can also be interpreted as the PDF of the distributed roughness elements), represents the porosity profile $\epsilon(k)$, see Altland (2022). Given that only positive values can be sampled from the Weibull PDF, we use the coordinate translation $y = \widetilde{k} - k_{\mathrm{min}}$, where k_{min} is the minimum roughness height which truncates the distribution. As long as $k_{\mathrm{min}} = 0$, the PDF from Eq. (A.4) can be integrated analytically yielding $\epsilon(k) = \epsilon(y)$, the wall-normal porosity profile. This is the case for $\epsilon(y=0) = 0$, which is the reason why we require the porosity values at the wall listed in Table 3. For the more general cases $\epsilon(y=0) \neq 0$, equivalent to $\epsilon(k_{\mathrm{min}}) \neq 0$, it is possible to calculate k_{min} for a prescribed porosity value solving from the analytical CDF, such that $k_{\mathrm{min}} = \left\{-\ln|1-\epsilon(y=0)|^{1/\phi}\right\}/\theta$. After k_{min} is obtained, we can use the transformation $\widetilde{k} = y + k_{\mathrm{min}}$, to find $\epsilon(y)$ from the analytical CDF,

$$\epsilon(y) = 1 - e^{-[\theta(y+k_{\mathrm{min}})]^{\phi}} \qquad \text{(statistical reconstruction)}. \tag{A.5}$$

In addition to $\epsilon(y)$, we also determine wall-normal profiles for the (averaged) equivalent diameter of the discrete roughness elements $D_{\circ}(y)$ and the equivalent flow (free area) pore diameter $D_k(y)$, noting $D_{\circ}(y) \neq D_k(y)$. Due to the shape of the discrete roughness elements as seen in Fig. 4, which correspond approximately to truncated conic elements, $D_{\circ} = \gamma k$, where γ is a constant scalar equal for all roughness elements and k is the average roughness height, obtained from the expected value of the one-point PDF of the roughness heights, i.e., a different PDF to that of $\mathcal{W}(\widetilde{k};\phi,\theta)$. We may consider the roughness heights conformal with a probabilistic fractal set, as long as a sufficiently large distribution of roughness heights exists, such that $k_{\mathrm{min}} \ll k_{\mathrm{max}}$, where k_{max} is a pre-specified maximum roughness height truncating the distribution. Conceptualizing roughness as a fractal set is not a new idea, see Majumdar and Bhushan (1990). Depending on whether $k_{\mathrm{min}} = 0$ or $k_{\mathrm{min}} > 0$, the roughness can be characterized as a probabilistic fractal by assuming a self-similar power law distribution of heights with upper, or lower and upper truncation, respectively, see Shen (2011). In the example case of lower and upper truncation, the PDF of the stochastic roughness heights k^* is

$$\psi(k^*) = \frac{Fk_{\mathrm{max}}^{-F}}{1-(k_{\mathrm{min}}/k_{\mathrm{max}})^F}\left(k^*\right)^{F-1}, \quad F > 0. \tag{A.6}$$

Here, F is a positive fractional exponent. This PDF has a mean value k which is the result of the converging integral $\int_{k_{\mathrm{min}}}^{k_{\mathrm{max}}} k^*\psi(k^*)\mathrm{d}k^*$, solvable analytically, see Shen (2011). Thus, with known values of k, k_{min} and k_{max}, it is possible to estimate F. We note that F is not necessarily the geometric fractal dimension. Rather, it is simply a fractal or fractional exponent which we take as a Korcak-law exponent, see Imre and Novotný (2016), in order to estimate the total number of roughness elements in the homogeneous surface as

$$N_T = \left(\frac{k_{\mathrm{max}}^2}{k_{\mathrm{min}}^2}\right)^F \qquad \text{(For probabilistic fractal sets)}. \tag{A.7}$$

Note that considering both $\mathcal{W}(\widetilde{k})$ and $\psi(k^*)$ is our equivalent interpretation of the need to consider both the PDF of roughness heights, $\psi(k^*)$, and their (horizonal-wavenumber) power spectrum related to $\mathcal{W}(\widetilde{k})$, as in Pérez-Ràfols and Almqvist (2019) and Yang et al. (2022). For

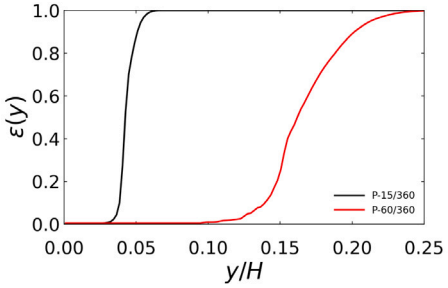

(a) Porosity profiles for cases P-15/360 and P-60/360

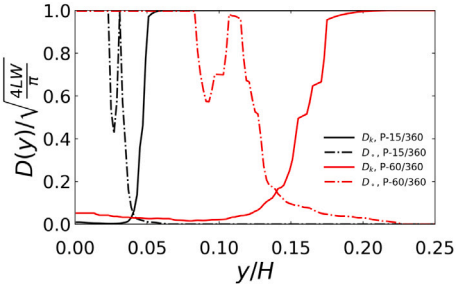

(b) Equivalent diameter profiles for cases P-15/360 and P-60/360

Fig. A.18. Homogeneous roughness surface parameterization in terms of porosity and equivalent diameters using the generalized method.

distributions of discrete roughness elements which do not conform with probabilistic fractal sets, such as case F-III, N_T must be specified as an input.

Consider now the total base-area of the roughness A_b given by $\Big(1-\epsilon(y=0)\Big)LW$, as the expected value of a distribution of roughness element diameters, i.e., $A_b = N_T(\pi/4)E\left[D_\circ^2(y=0)\right]$. Given the assumed shape of the roughness elements in Fig. 4, we can calculate the roughness element aspect ratio γ as

$$\gamma = \sqrt{\frac{4LW\,(1-\epsilon(y=0))}{\pi N_T \int_{k_{\min}}^{k_{\max}} \left\{(k^*)^2\,\psi(k^*)\right\} \mathrm{d}k^*}}. \tag{A.8}$$

Note that $\int_{k_{\min}}^{k_{\max}} \left\{(k^*)^2\,\psi(k^*)\right\} \mathrm{d}k^*$ is simplified to k^2 for the constant height roughness elements of case F-III. This allows then the determination of $D_\circ(y)$ and $D_k(y)$ as

$$D_\circ(y) = \gamma k - 0.9\gamma y, \qquad D_k(y) = \sqrt{\frac{4LW\epsilon(y)}{\pi N_T}}. \tag{A.9}$$

Since the distribution $\psi(k^*)$ allows heights $k^* > k$, but $D_\circ(y)$ from Eq. (A.9) is only valid for $y \le k$, we superpose in such cases an exponential decay in the range $k < y \le k_{\max}$, such that $D_\circ(k_{\max}) \to 0$; in fact, we take $D_\circ(k_{\max})$ as 1% of $D_\circ(y=k)$.

Fig. A.19(a) shows the determined porosity profiles for the cases with regular roughness. It is seen that the Weibull CDF approximation for the porosity given by Eq. (A.5) observes important deviations with respect to the published surface porosity profile in Forooghi et al. (2018). Given that the calculation method for the drag forcing coefficients suggested in this work is very different to that in Forooghi et al. (2018), we do not comment further in this regard. Fig. A.19(b) shows the determined equivalent diameter profiles for the cases with regular roughness. Unlike the porosity profiles shown in Fig. A.19(a), there is no available data for comparison of these results.

Appendix B. Calculation of the ODT kernel coefficients

Next, we explain the calculation of the kernel coefficient c_i (for $i \in \{1,2,3\}$, i.e., i corresponding to the index of each velocity component). The coefficient c_i is associated to the kinetic energy redistribution procedure during an eddy event, and modifies mapped profiles as per Eq. (21). The procedure detailed here is different to a previous implementation of drag effects in ODT (Freire and Chamecki, 2018), although it follows the same motivation. The difference with respect to Freire and Chamecki (2018) is simply due to the chosen form of the drag forcing, and the rationale used to calculate the change in kinetic energy due to drag. We consider the wall-normal drag forcing component, $f_{p,2}$, which is not implemented in Eq. (24), as the missing drag force (density) contributing to the wall-normal advecting velocity responsible for the Reynolds stress (or turbulent advection). This drag effect causes a loss of kinetic energy during eddy events, some $\Delta e_K = \Delta e_d < 0$, such that

$$\Delta e_d = \sum_i^3 \left\{ \frac{1}{2}\int_l \left[u_i(t_e, f(y)) + c_i K(y)\right]^2 \mathrm{d}y - \frac{1}{2}\int_l u_i^2(t_e, y)\,\mathrm{d}y \right\}. \tag{B.1}$$

Consider now $\Delta e_{K,i}$ as a change of kinetic energy in each velocity component on the absence of drag, and $\Delta e_{d,i}$ as a drag loss in each velocity component, such that $\sum_i^3 \Delta e_{K,i} = \Delta e_K = \sum_i^3 \Delta e_{d,i} = \Delta e_d$. Assuming that $\Delta e_{K,i}$ and $\Delta e_{d,i}$ are of the same sign, which would be a typical situation for the streamwise velocity component $i = 1$, the energy change for the ith velocity component is

$$\Delta e_{K,i} + \Delta e_{d,i} = \frac{1}{2}\int_l \left[u_i(t_e, f(y)) + c_i K(y)\right]^2 \mathrm{d}y - \frac{1}{2}\int_l u_i^2(t_e, y)\,\mathrm{d}y. \tag{B.2}$$

Define now the following quantities,

$$P_i = \int_l u_i K(y)\mathrm{d}y, \qquad T = \frac{1}{2}\int_l K^2(y)\mathrm{d}y, \tag{B.3}$$

such that Eq. (B.2) can be rewritten as

$$c_i^2 T + c_i P_i - \left(\Delta e_{K,i} + \Delta e_{d,i}\right) = 0. \tag{B.4}$$

This is a quadratic equation on c_i which has some (analytically obtainable) minimum $c_{i,\min} = -P_i/(2T)$, see Kerstein et al. (2001). We relate $c_{i,\min}$ to some minimum kinetic energy change per velocity component $\Delta e_{K,i,\min} = -Q_i$, i.e., a maximum extractable kinetic energy in the eddy event. Thus, we can obtain by substitution of $c_{i,\min}$ in Eq. (B.4),

$$Q_i = \Delta e_{d,i} + \frac{P_i^2}{4T}. \tag{B.5}$$

The fraction of Q_i which is redistributed depends on one ODT model parameter, $\alpha \le 1$, which is introduced to represent the tendency of the pressure to restore isotropy on the absence of shear and body forces in incompressible flow, see Kerstein et al. (2001),

$$\Delta e_{K,i,\min} = -\alpha Q_i + \frac{1}{2}\sum_{j\neq i}^{3} \alpha Q_j. \tag{B.6}$$

We always use $\alpha = 2/3$ implying uniform redistribution of extractable kinetic energy during the eddy event. Solution of the quadratic Eq. (B.4) for any c_i is then, upon substitution of Eqs. (B.5) and (B.6),

$$c_i = \frac{-P_i \pm \sqrt{(1-\alpha)\,P_i^2 + \frac{1}{2}\sum_{j\neq i}^3 \alpha P_j^2 + 4T\left[(1-\alpha)\,\Delta e_{d,i} + \frac{1}{2}\sum_{j\neq i}^3 \alpha \Delta e_{d,j}\right]}}{2T}. \tag{B.7}$$

In order to resolve the sign ambiguity from the square root term, and considering that α is the parameter governing energy redistribution due to c_i, we impose the condition $c_i \to 0$ whenever $\alpha \to 0$ and $\Delta e_{d,i} \to 0$. Thus, in Eq. (B.7), we take the sign of the square root term as the sign of P_i. We also note that for the chosen $\alpha = 2/3$, considering that

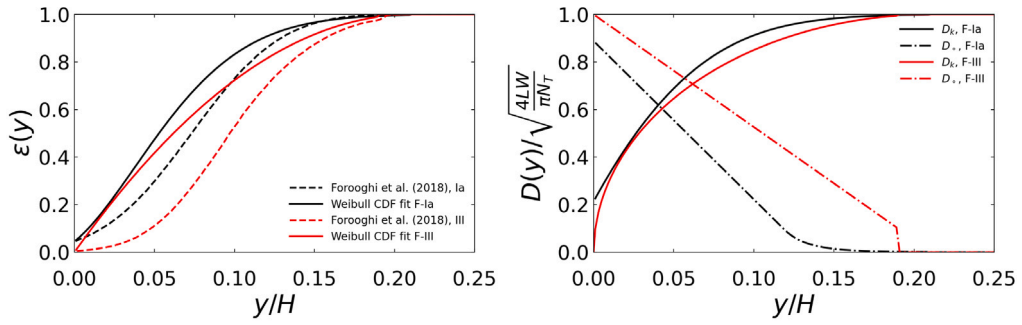

(a) Porosity profiles for cases F-Ia and F-III (b) Equivalent diameter profiles for cases F-Ia and F-III

Fig. A.19. Homogeneous roughness surface reconstruction (porosity and equivalent diameters) using statistical moments of the roughness distribution. The porosity profiles available in Forooghi et al. (2018) are shown for reference in (a) for said cases.

$\sum_i^3 \Delta e_{d,i} = \Delta e_d$, the expression can be simplified to

$$c_i = \frac{-P_i \pm \sqrt{\frac{1}{3}\sum_i^3 P_i^2 + 4T\left(\frac{1}{3}\Delta e_d\right)}}{2T}. \tag{B.8}$$

This imposes the condition $\Delta e_d > -\sum_i^3 P_i^2/(4T)$. Note concerning $\Delta e_{d,i}$, that the assumption $\alpha = 2/3$ is equivalent to an assumption $\Delta e_{d,i} = \Delta e_d/3$.

Finally, we discuss the calculation of Δe_d. To that extent, we calculate the kinetic energy equation resulting from Eq. (24), using all drag force components (including $f_{p,2}$, although omitting the pressure term from the inhomogeneous term $\mathcal{I}_2$), as well as the standard definition of the magnitude of the velocity vector. This is

$$\begin{aligned}\frac{\partial\left(\frac{1}{2}\langle u_i\rangle^2\right)}{\partial t} + \frac{1}{2}\mathcal{M}(\langle u_i\rangle^2) = &-\frac{1}{\rho}\langle u_i\rangle\frac{\mathrm{d}\overline{p}}{\mathrm{d}x}\delta_{i1} + \nu\frac{\partial^2\left(\frac{1}{2}\langle u_i\rangle^2\right)}{\partial y^2} - \nu\left(\frac{\partial\langle u_i\rangle}{\partial y}\right)^2 \\ &- \frac{\nu\epsilon N_T\pi D_\circ}{D_k^2 W}\hat{c}_I\langle u_i\rangle^2 - \frac{\epsilon N_T\pi D_\circ}{D_k W}\hat{c}_{II}\|\langle u_i\rangle\|\langle u_i\rangle^2 \\ &- \frac{\epsilon N_T\pi D_\circ}{\nu W}\hat{c}_{III}\|\langle u_i\rangle\|^2\langle u_i\rangle^2 + \langle u_i\rangle\mathcal{I}_i.\end{aligned} \tag{B.9}$$

Recall that square terms in this expression are equivalent to scalar product multiplications $u_i u_i$ which eliminate component indices due to Einstein summation rules. We consider the usual vector magnitude evaluation for the operator $\|\cdot\|$. From this kinetic energy equation, we only consider the Forchheimer-like term of the drag as our model representation for Δe_d, i.e., the term observing $\|\langle u_i\rangle\|\langle u_i\rangle^2$. This is because the Forchheimer-like term corresponds to pressure or form drag, and as such, it is the most natural term to consider for a pressure-scrambling effect contribution. The Darcy-like term corresponds to viscous drag, and as such, should be observed during the deterministic time integration of Eq. (24) in the ODT advancement. Note also that the inhomogeneous term $\langle u_i\rangle\mathcal{I}_i$ may be interpreted as a modification to the viscous transport term of kinetic energy, and to the Darcy-like term. The transitional regime term of the drag is neglected in the analysis, given that all values observed for $\hat{c}_{III}$ are close to zero. Observing the previous considerations, Δe_d during an arbitrary eddy event occurring in the interval $t = [0, \Delta t_l]$ is defined as

$$\Delta e_d = \frac{1}{2}\int_l \langle u_i\rangle^2(y,\Delta t_l)\,\mathrm{d}y - \frac{1}{2}\int_l \langle u_i\rangle^2(y,0)\,\mathrm{d}y, \tag{B.10}$$

where the kinetic energy before and after the eddy event (in a time interval equivalent to the eddy turnover time Δt_l) should be given by the corresponding contribution in Eq. (B.9), that is, the form or pressure drag term on the kinetic energy equation. Define $e_d^{*,1/2} = \|\langle u_i\rangle\|$, and

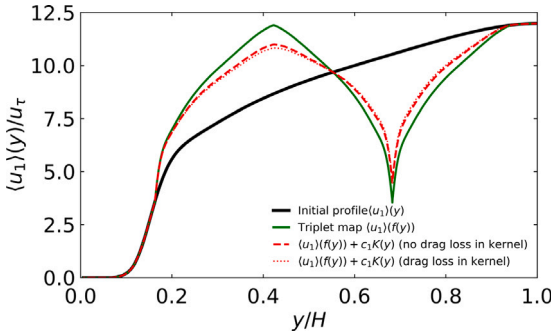

Fig. B.20. Instantaneous eddy event implementation on an initial condition similar to the converged mean velocity profile of one of the study cases discussed in the text. The figure shows the implementation of the triplet map, together with superimposed kernels considering or neglecting the drag loss term Δe_d.

note $\langle u_i\rangle^2 = \|\langle u_i\rangle\|^2 = e_d^*$ according to scalar product rules. We can then write the form or pressure drag contribution on Eq. (B.9), as an ordinary differential equation for every coordinate y,

$$\frac{\mathrm{d}e_d^*}{\mathrm{d}t} = -2\frac{\epsilon N_T\pi D_\circ}{D_k W}\hat{c}_{II}e_d^{*,3/2}. \tag{B.11}$$

This equation can be integrated analytically in time, using initial conditions $e_d^*(y,0) = \langle u_i\rangle(y,0)\langle u_i\rangle(y,0)$. The solution is

$$e_d^*(y,\Delta t_l) = \frac{e_d^*(y,0)}{\left[1 + e_d^{*,1/2}(y,0)\frac{\epsilon N_T\pi D_\circ}{D_k W}\hat{c}_{II}(y)\Delta t_l\right]^2}. \tag{B.12}$$

The corresponding substitution on Eq. (B.10) leads to the definition of Δe_d,

$$\Delta e_d = \frac{1}{2}\int_l \frac{e_d^*(y,0)}{\left[1 + e_d^{*,1/2}(y,0)\frac{\epsilon N_T\pi D_\circ}{D_k W}\hat{c}_{II}(y)\Delta t_l\right]^2}\mathrm{d}y - \frac{1}{2}\int_l e_d^*(y,0)\,\mathrm{d}y. \tag{B.13}$$

Recall the condition $\Delta e_d > -\sum_i^3 P_i^2/(4T)$ in order to find real solutions for the kernel coefficients. If the calculation of Δe_d by Eq. (B.13) does not satisfy the determinant condition for the calculation of the kernel coefficients, the kernel drag loss is ignored. Fig. B.20 shows an example of the implementation of an eddy event on an initial condition similar to the converged mean velocity profile of one of the study cases discussed in the text. There is only a minor effect of the drag loss term Δe_d on the kernel implementation procedure.

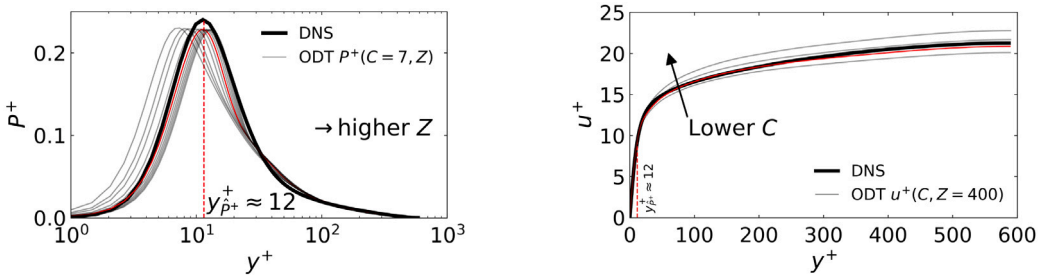

(a) Effects of ODT model parameter Z on TKE production P^+

(b) Effects of ODT model parameter C on the mean velocity profile

Fig. C.21. Effects of ODT model parameters C and Z in a smooth wall turbulent channel flow with $\mathrm{Re}_\tau = 590$. Gray lines show ODT simulation results with different choices of model parameters. The red line shows the ODT simulation with optimal parameter values. The thick black line corresponds to reference DNS data taken from Moser et al. (1999). (For interpretation of the references to color in this figure legend, the reader is referred to the web version of this article.)

We remark an issue concerning the drag loss term contributions in eddy events. To that extent, it is important to stress that the drag loss contribution is considered for the calculation of the kernel coefficients c_i, but it is not considered for the purpose of the calculation of the eddy turnover time Δt_l in Eq. (22). The viscous drag is considered to be incorporated in the viscous penalty term represented by the model parameter Z in ODT. The form drag is considered to affect only inter-component energy transfer, and thus, it determines the calculation of the kernel coefficients, but does not modify the probability of occurrence of an eddy.

Appendix C. Effect of ODT model parameters in smooth-wall turbulent channel flows

We comment now on the effect of the ODT model parameters C and Z in smooth-wall turbulent channel flows. Fig. C.21(a) shows the effect of Z on the TKE production P^+. It is notable that a change in Z causes a shift in the peak of production $\hat{P}^+$, and to that extent, there is only one correct value of Z. Most notably, and as seen in Eq. (22), Z has the form of the square of a local Reynolds number, or conversely, of a viscous coordinate. For smooth wall turbulent channel flows, it is remarkable that $\sqrt{Z}$ coincides with the viscous coordinate $y^+_{\hat{P}} \approx 12$ multiplied by the corresponding local production to dissipation ratio $\hat{P}/D_{\hat{P}} \approx 5/3$. Based on these observations, Z is mostly insensitive to Re_τ effects, partly because $y^+_{\hat{P}}$ and $\hat{P}/D_{\hat{P}}$ are mostly insensitive to Re_τ, see Laadhari (2002). Fig. C.21(b) shows the effect of C on the mean streamwise velocity profile $u^+(y^+)$. There is an optimal choice of C for the best fit of the mean velocity profile, which could also be interpreted as the optimal choice for the correct reproduction of the skin friction coefficient C_f, at least when comparing with DNS data. Note that asymptotically larger values of C cause asymptotically smaller effects on C_f.

Appendix D. Supplementary data

A document containing a step-by-step derivation of the DANS velocity equation, i.e., Eqs. (5) and (9), is attached as supplementary material to this article. The repository (Medina Méndez, 2025) contains scripts for the generation of the wall-normal roughness drag coefficients. Simulation data is also included in the repository, and is available for download. A freely available version of ODT maintained by Prof. David Lignell, fully capable of simulating smooth wall turbulent channel flow can be accessed in the repository https://github.com/BYUignite/ODT. The ODT simulation code for turbulent channel flow with rough walls is not included in the repository, but it can be provided upon request.

Supplementary material related to this article can be found online at https://doi.org/10.1016/j.ijheatfluidflow.2025.110113.

Data availability

The link to the repository containing supplementary material and data has been added as a reference in the article.

References

Altland, S., 2022. A Distributed Element Roughness Model Based on the Double Averaged Navier–Stokes Equations (Ph.D. thesis).

Aupoix, B., 2015. Revisiting the discrete element method for predictions of flows over rough surfaces. J. Fluids Eng. 138, 031205. http://dx.doi.org/10.1115/1.4031558.

Breugem, W.P., 2005. The Influence of Wall Permeability on Laminar and Turbulent Flows Theory and Simulations (Ph.D. thesis).

Breugem, W.P., Boersma, B.J., Uittenbogaard, R.E., 2006. The influence of wall permeability on turbulent channel flow. J. Fluid Mech. 562, 35–72. http://dx.doi.org/10.1017/S0022112006000887.

Busse, A., Lützner, M., Sandham, N.D., 2015. Direct numerical simulation of turbulent flow over a rough surface based on a surface scan. Comput. & Fluids 116, 129–147. http://dx.doi.org/10.1016/j.compfluid.2015.04.008.

Busse, A., Sandham, N.D., 2012. Parametric forcing approach to rough-wall turbulent channel flow. J. Fluid Mech. 712, 169–202. http://dx.doi.org/10.1017/jfm.2012.408.

Busse, A., Thakkar, M., Sandham, N.D., 2017. Reynolds-number dependence of the near-wall flow over irregular rough surfaces. J. Fluid Mech. 810, 196–224. http://dx.doi.org/10.1017/jfm.2016.680.

Chan, L., MacDonald, M., Chung, D., Hutchins, N., Ooi, A., 2015. A systematic investigation of roughness height and wavelength in turbulent pipe flow in the transitionally rough regime. J. Fluid Mech. 771, 743–777. http://dx.doi.org/10.1017/jfm.2015.172.

Chan-Braun, C., García-Villalba, M., Uhlmann, M., 2011. Force and torque acting on particles in a transitionally rough open-channel flow. J. Fluid Mech. 684, 441–474. http://dx.doi.org/10.1017/jfm.2011.311.

Chandesris, M., Jamet, D., 2006. Boundary conditions at a planar fluid–porous interface for a poiseuille flow. Int. J. Heat Mass Transfer 49, 2137–2150. http://dx.doi.org/10.1016/j.ijheatmasstransfer.2005.12.010.

Chedevergne, F., 2021. A double-averaged Navier–Stokes $k-\omega$ turbulence model for wall flows over rough surfaces with heat transfer. J. Turbul. 22, 713–734. http://dx.doi.org/10.1080/14685248.2021.1973014.

Chedevergne, F., Yang, J., Stroh, A., Forooghi, P., 2025. Analysis of separation in the roughness sublayer using DNS data and DANS/DEM modelling of roughness effects. Flow Turbul. Combust. 114, 713–735. http://dx.doi.org/10.1007/s10494-024-00585-9.

Chorin, A.J., 1986. Turbulence and vortex stretching on a lattice. Commun. Pure Appl. Math. 39, http://dx.doi.org/10.1002/cpa.3160390706.

Chung, D., Hutchins, N., Schultz, M.P., Flack, K.A., 2021. Predicting the drag of rough surfaces. Annu. Rev. Fluid Mech. 53, 439–471. http://dx.doi.org/10.1146/annurev-fluid-062520-115127.

Cooke, J., Jerolmack, D., Park, G.I., 2024. Mesoscale structure of the atmospheric boundary layer across a natural roughness transition. PNAS 121, e2320216121. http://dx.doi.org/10.1073/pnas.2320216121.

Firdaouss, M., Guermond, J.L., Le Quéré, P., 1997. Nonlinear corrections to Darcy's law at low Reynolds numbers. J. Fluid Mech. 343, 331–350. http://dx.doi.org/10.1017/S0022112097005843.

Flack, K.A., Schultz, M.P., Barros, J.M., 2020a. Skin friction measurements of systematically-varied roughness: Probing the role of roughness amplitude and skewness. Flow Turbul. Combust. 104, 317–329. http://dx.doi.org/10.1007/s10494-019-00077-1.

Flack, K.A., Schultz, M.P., Volino, R.J., 2020b. The effect of a systematic change in surface roughness skewness on turbulence and drag. Int. J. Heat Fluid Flow 85, 108669. http://dx.doi.org/10.1016/j.ijheatfluidflow.2020.108669.

Forooghi, P., Frohnapfel, B., Magagnato, F., Busse, A., 2018. A modified parametric forcing approach for modelling of roughness. Int. J. Heat Fluid Flow 71, 200–209. http://dx.doi.org/10.1016/j.ijheatfluidflow.2018.03.019.

Forooghi, P., Stroh, A., Magagnato, F., Jakirlić, S., Frohnapfel, B., 2017. Toward a universal roughness correlation. J. Fluids Eng. 139, http://dx.doi.org/10.1115/1.4037280.

Freire, L.S., Chamecki, M., 2018. A one-dimensional stochastic model of turbulence within and above plant canopies. Agric. For. Meteorol. 250–251, 9–23. http://dx.doi.org/10.1016/j.agrformet.2017.12.211.

Freire, L.S., Chamecki, M., 2021. Large-eddy simulation of smooth and rough channel flows using a one-dimensional stochastic wall model. Comput. & Fluids 230, 105135. http://dx.doi.org/10.1016/j.compfluid.2021.105135.

Hanson, D.R., Kinzel, M.P., McClain, S.T., 2019. Validation of the discrete element roughness method for predicting heat transfer on rough surfaces. Int. J. Heat Mass Transfer 136, 1217–1232. http://dx.doi.org/10.1016/j.ijheatmasstransfer.2019.03.062.

Imre, A.R., Novotný, J., 2016. Fractals and the Korcak-law: a history and a correction. Eur. Phys. J. H 41, 69–91. http://dx.doi.org/10.1140/epjh/e2016-60039-8.

Jackson, P.S., 1981. On the displacement height in the logarithmic velocity profile. J. Fluid Mech. 111, 15–25. http://dx.doi.org/10.1017/S0022112081002279.

Jelly, T.O., Busse, A., 2019. Reynolds number dependence of Reynolds and dispersive stresses in turbulent channel flow past irregular near-Gaussian roughness. Int. J. Heat Fluid Flow 80, 108485. http://dx.doi.org/10.1016/j.ijheatfluidflow.2019.108485.

Kadivar, M., Tormey, D., McGranaghan, G., 2021. A review on turbulent flow over rough surfaces: Fundamentals and theories. Int. J. Thermofluids 10, 100077. http://dx.doi.org/10.1016/j.ijft.2021.100077.

Kerstein, A.R., 1999. One-dimensional turbulence: model formulation and application to homogeneous turbulence, shear flows, and buoyant stratified flows. J. Fluid Mech. 392, 277–334. http://dx.doi.org/10.1017/S0022112099005376.

Kerstein, A.R., Ashurst, W.T., Wunsch, S., Nilsen, V., 2001. One-dimensional turbulence: Vector formulation and application to free-shear flows. J. Fluid Mech. 447, 85–109. http://dx.doi.org/10.1017/S0022112001005778.

Khalifa, Z., Pocher, L., Tilton, N., 2020. Regimes of flow through cylinder arrays subject to steady pressure gradients. Int. J. Heat Mass Transfer 159, 120072. http://dx.doi.org/10.1016/j.ijheatmasstransfer.2020.120072.

Klein, M., Schmidt, H., Lignell, D.O., 2022. Stochastic modeling of surface scalar-flux fluctuations in turbulent channel flow using one-dimensional turbulence. Int. J. Heat Fluid Flow 93, 108889. http://dx.doi.org/10.1016/j.ijheatfluidflow.2021.108889.

Laadhari, F., 2002. On the evolution of maximum turbulent kinetic energy production in a channel flow. Phys. Fluids 14, L65–L68. http://dx.doi.org/10.1063/1.1511731.

Lee, M., Moser, R., 2015. Direct numerical simulation of turbulent channel flow up to Ret = 5200. J. Fluid Mech. 774, 395–415. http://dx.doi.org/10.1017/jfm.2015.268.

Lignell, D., Kerstein, A.R., Sun, G., Monson, E., 2013. Mesh adaption for efficient multiscale implementation of one-dimensional turbulence. Theor. Comput. Fluid Dyn. 27, 273–295. http://dx.doi.org/10.1007/s00162-012-0267-9.

Lignell, D., Lansinger, V.B., Medina Méndez, J.A., Klein, M., Kerstein, A.R., Schmidt, H., Fistler, M., Oevermann, M., 2018. One-dimensional turbulence modeling for cylindrical and spherical flows: model formulation and application. Theor. Comput. Fluid Dyn. 32, 495–520. http://dx.doi.org/10.1007/s00162-018-0465-1.

Majumdar, A., Bhushan, B., 1990. Role of fractal geometry in roughness characterization and contact mechanics of surfaces. J. Tribol. 112, 205–216. http://dx.doi.org/10.1115/1.2920243.

McClain, S.T., Brown, J.M., 2009. Reduced rough-surface parametrization for use with the discrete-element model. J. Turbomach. 131, 021020. http://dx.doi.org/10.1115/1.2952379.

McDermott, R., 2005. Towards One-Dimensional Turbulence Subgrid Closure for Large-Eddy Simulation (Ph.D. thesis). University of Utah.

Medina Méndez, J.A., 2025. Roughness drag parameterization framework for use in the one-dimensional turbulence model. http://dx.doi.org/10.5281/zenodo.14713216.

Mei, C.C., Auriault, J.L., 1991. The effect of weak inertia on flow through a porous medium. J. Fluid Mech. 222, 647–663. http://dx.doi.org/10.1017/S0022112091001258.

Mignot, E., Barthélemy, E., Hurther, D., 2008. Turbulent kinetic energy budget in a gravel-bed channel flow. Acta Geophys. 56, 601–613. http://dx.doi.org/10.2478/s11600-008-0020-3.

Mittal, R., Iaccarino, G., 2005. Immersed boundary methods. Annu. Rev. Fluid Mech. 37, 239–261. http://dx.doi.org/10.1146/annurev.fluid.37.061903.175743.

Moser, R., Kim, J., Mansour, N., 1999. Direct numerical simulation of turbulent channel flow up to Ret = 590. Phys. Fluids 11, 943–945. http://dx.doi.org/10.1063/1.869966.

Nikuradse, J., 1933. Strömungsgesetze in Rauhen Rohren. VDI-Forschungsheft, p. 361.

Ottino, J.M., Jana, S.C., Chakravarthy, V.S., 1994. From Reynolds's stretching and folding to mixing studies using horseshoe maps. Phys. Fluids 6, 685–699. http://dx.doi.org/10.1063/1.868308.

Peeters, J., Sandham, N., 2019. Turbulent heat transfer in channels with irregular roughness. Int. J. Heat Mass Transfer 138, 454–467. http://dx.doi.org/10.1016/j.ijheatmasstransfer.2019.04.013.

Pérez-Ràfols, F., Almqvist, A., 2019. Generating randomly rough surfaces with given height probability distribution and power spectrum. Tribol. Int. 131, 591–604. http://dx.doi.org/10.1016/j.triboint.2018.11.020.

Pope, S.B., 2001. Turbulent Flows. IOP Publishing.

Schlichting, H., 1937. Experimental Investigation of the Problem of Surface Roughness. Technical Report 823.

Schultz, M.P., Flack, K.A., 2009. Turbulent boundary layers on a systematically varied rough wall. Phys. Fluids 21, 015104. http://dx.doi.org/10.1063/1.3059630.

Shen, W., 2011. Fractal invariable distribution and its application in large-sized and super large-sized mineral deposits. Geosci. Front. 2, 87–91. http://dx.doi.org/10.1016/j.gsf.2010.11.003.

Sturman, R., 2012. The Role of Discontinuities in Mixing. In: Adv. Appl. Mech., vol. 45, Elsevier, pp. 51–90. http://dx.doi.org/10.1016/B978-0-12-380876-9.00002-1.

Thakkar, M., Busse, A., Sandham, N.D., 2017. Surface correlations of hydrodynamic drag for transitionally rough engineering surfaces. J. Turbul. 18, 138–169. http://dx.doi.org/10.1080/14685248.2016.1258119.

Thorat, U., Jones, M., Woollam, R., Owen, J., Barker, R., Thompson, H., de Boer, G., 2024. Computational fluid dynamics driven mass transfer model for the prediction of CO2 corrosion in pipelines. J. Pipeline Sci. Eng. 4, 100148. http://dx.doi.org/10.1016/j.jpse.2023.100148.

Toja-Silva, F., Kono, T., Peralta, C., Lopez-Garcia, O., Chen, J., 2018. A review of computational fluid dynamics (CFD) simulations of the wind flow around buildings for urban wind energy exploitation. J. Wind Eng. Ind. Aerodyn. 180, 66–87. http://dx.doi.org/10.1016/j.jweia.2018.07.010.

Toussaint, D., Chedevergne, F., Léon, O., 2020. Analysis of the different sources of stress acting in fully rough turbulent flows over geometrical roughness elements. Phys. Fluids 32, 075107. http://dx.doi.org/10.1063/5.0010771.

Whitaker, S., 1996. The Forchheimer equation: A theoretical development. Transp. Porous Media 25, 27–61. http://dx.doi.org/10.1007/BF00141261.

Whitaker, S., 1999. The Method of Volume Averaging. Vol. 13, Springer Science & Business Media, http://dx.doi.org/10.1007/978-94-017-3389-2.

Wilcox, D.C., 2006. Turbulence Modeling for CFD. DCW Industries, Inc., La Cañada, California, USA.

Yang, J., Stroh, A., Chung, D., Forooghi, P., 2022. Direct numerical simulation-based characterization of pseudo-random roughness in minimal channels. J. Fluid Mech. 941 (A47), http://dx.doi.org/10.1017/jfm.2022.331.

Yuan, J., Piomelli, U., 2014. Roughness effects on the Reynolds stress budgets in near-wall turbulence. J. Fluid Mech. 760 (R1), http://dx.doi.org/10.1017/jfm.2014.608.